thermo

MDPI

Article

CFD Assessment of Thermal Comfort and Heating Demand in Courtrooms Under Envelope Retrofit Scenarios

Cătălin Ciprian Vulpe [1], Florin-Emilian Țurcanu [2,*], Valeriu-Sebastian Hudișteanu [2], Cristian-Nelu Cherecheș [2], Claudiu Romila [3], Cătălin Onuțu [1], Dragoș Ungureanu [1], Adrian Alexandru Șerbănoiu [1] and Cătălin George Popovici [2]

[1] Department of Concrete Structures, Building Materials, Technology and Management, Faculty of Civil Engineering and Building Services, "Gheorghe Asachi" Technical University of Iași, 1 Prof. Dimitrie Mangeron Blvd., 700050 Iași, Romania; catalin-ciprian.vulpe@student.tuiasi.ro (C.C.V.); onutu.catalin@yahoo.com (C.O.); dragos.ungureanu@academic.tuiasi.ro (D.U.); adrian-alexandru.serbanoiu@academic.tuiasi.ro (A.A.Ș.)

[2] Department of Building Services, Faculty of Civil Engineering and Building Services, "Gheorghe Asachi" Technical University of Iași, 1 Prof. Dimitrie Mangeron Blvd., 700050 Iași, Romania; valeriu-sebastian.hudisteanu@academic.tuiasi.ro (V.-S.H.); nelu.chereches@academic.tuiasi.ro (C.-N.C.); catalinpopovici@climatherm.ro (C.G.P.)

[3] Department of Civil and Industrial Engineering, Faculty of Civil Engineering and Building Services, "Gheorghe Asachi" Technical University of Iași, 1 Prof. Dimitrie Mangeron Blvd., 700050 Iași, Romania; claudiu.romila@academic.tuiasi.ro

* Correspondence: florin-emilian.turcanu@academic.tuiasi.ro

Abstract

Courtrooms are tall rooms in which cold glazing, radiator plumes and stratification shape winter comfort. We combined infrared thermography with steady CFD including surface radiation and a coupled envelope (OpenFOAM, cross-checked with Ansys Fluent) to assess window replacement and wall insulation in three courtrooms in Iași, Romania, at −18 °C outdoors. The model was verified on three meshes and tested against a downdraught correlation and measured air temperatures; after calibration of the unknown heat input, it underestimated the air temperature of two further periods by 1.2–1.7 K. The mean PMV stayed between −0.07 and 0.04 and the mean draught rate below 8%, but the radiators did not prevent downdraught: the ankle-level draught rate in the first seat row reached 24–29%, above the 20% limit of category B, and 18–24% after wall insulation. Window replacement cut the transmission loss by 13–21%, and, with wall insulation, by 39–75%, after which ventilation becomes the largest loss. Supply air at 12 °C after heat recovery caused draught in a fifth of the occupied zone. Envelope retrofit should therefore come with demand-controlled ventilation, enthalpy recovery and supply air reheated close to room temperature.

Keywords: courtroom; computational fluid dynamics (CFD); OpenFOAM; thermal comfort; energy retrofit; draught; surface radiation; downdraught

Academic Editor: Gerardo Maria Mauro

Received: 22 October 2026
Revised: 16 November 2026
Accepted: 19 November 2026
Published: 23 November 2026

Copyright: © 2026 by the author. Licensee MDPI, Basel, Switzerland. This article is an open access article distributed under the terms and conditions of the Creative Commons Attribution (CC BY) license.

1. Introduction

European energy policy makes the renovation of public buildings a priority: the recast Energy Performance of Buildings Directive and the Energy Efficiency Directive require public bodies to renovate a share of their floor area each year and to bring the build-

ing stock to zero-emission levels [1,2]. Renovation decisions rest on expected energy savings, and the indoor climate is judged with single-zone indicators. Tall rooms heated by radiators are far from uniform: cold windows generate downdraughts, radiators create plumes and the air stratifies, so the occupied zone can differ from the mean room temperature [3–5].

A cold vertical surface cools the adjacent air, which accelerates downward and spreads over the floor as a cold layer. Heiselberg [3] related the peak velocity of this layer to the surface-to-air temperature difference and the surface height. Radiators under the windows are the classical remedy, because their plumes oppose the descending flow, and studies have examined which radiator type, position and temperature limit draught risk [4,6–8]. Window replacement raises the glazing temperature and weakens the downdraught, but it also lowers the radiator output required, so the two effects interact.

Researchers have used computational fluid dynamics (CFD) for more than five decades to predict air distribution and thermal comfort in rooms [9,10], and comfort studies rely more and more on open-source codes such as OpenFOAM [11,12]. For tall public rooms, CFD studies concern mainly churches, where the heating system sets the comfort in the occupied zone [13,14]. Recent studies applied CFD to the retrofit of heritage and public buildings [15,16], and one examined winter air-supply strategies in a traditional judicial building [17]. Courtrooms add their own features—they are tall and people sit in them for hours—and a parallel monitoring campaign in Iași found them overheated and very dry in winter. Other courthouse studies dealt with mould, ventilation and infection risk [18,19] or with energy use [20,21].

The credibility of such simulations depends on the modelling choices and on how they are checked. Steady Reynolds-averaged (RANS) models, mostly of the k–ε family, remain the practical choice for room airflow [22–24], but model performance depends on the flow case [25], and RANS models differ in the boundary-layer thickness at a cold window [26]. Room CFD with prescribed surface temperatures often omits surface radiation, although radiative exchange governs the mean radiant temperature, which varies with position in the room and with the U-values of wall and window [27]; radiant asymmetry near cold surfaces is a local discomfort parameter of its own [28]. Guidelines for indoor CFD therefore ask authors to report the turbulence model, boundary conditions, schemes and grid [29]; to separate verification (solving the equations correctly) from validation (solving the right equations, tested against measurements) [30,31]; and to quantify the discretisation error [32].

In this paper we use infrared thermography and three-dimensional CFD to assess how window replacement and external wall insulation change the heating demand and the thermal comfort in the occupied zone of three courtrooms in Iași, Romania. The study adds three elements to existing work. First, it treats courtrooms as a building type with specific geometry, occupancy and winter operation. Second, it couples the room airflow with surface radiation and a thermally coupled envelope, and it compares the retrofit scenarios under this model with ventilation cases. Third, it tests the model stepwise: grid and iterative verification, a code-to-code comparison, sensitivity to the turbulence model and the radiator representation, and a partial validation against a downdraught correlation and measured air temperatures. The validation is partial and the envelope data are assumed, so we treat the draught indicators as indicative and report their uncertainty (limits in Section 3.9).

2. Materials and Methods

2.1. Buildings, Rooms and Geometry

The Court of Appeal and the Tribunal of Iași share a recent multi-storey building with a ventilated façade (mineral wool insulation behind aluminium composite panels) and aluminium-framed windows. The District Court occupies an older building, for which we assumed an uninsulated masonry envelope. We selected three hearing rooms with different geometry and exposure from the rooms monitored in winter 2025 (Table 1): Room 5 of the Court of Appeal (CA-R5), a 4.9 m-high room with two exterior walls and a wooden court platform; Room 8 of the Tribunal (TR-R8), a corner room with three exterior walls; and Room 6 of the District Court (DC-R6), a long room with windows on two opposite walls. Hand-drawn survey sketches gave the plan dimensions, clear heights and positions of windows, doors and radiators, which we converted into parametric three-dimensional models (Figure 1). Where the survey did not record window and radiator dimensions, we used typical values (windowsill 1.0 m and height 2.6 m in the tall rooms, 0.9 m and 2.0 m in DC-R6; radiators 0.6 m high, 0.15 m above the floor, under each window).

Table 1. Geometry of the simulated courtrooms (number of cells for the 0.15 m mesh).

Room	W × L × H [m]	Floor Area [m²]	Exterior Walls	$A_{wall,ext}$ [m²]	A_{window} [m²]	Radiators	Cells
CA-R5	8.42 × 10.9 × 4.91	92	W, N	83.38	11.48	3	134,904
DC-R6	6.6 × 13.535 × 3.85	89	N, S	41.46	9.36	4	102,960
TR-R8	8.68 × 10.4 × 4.8	90	N, E, W	128.50	13.00	4	128,064

The exterior wall area includes the wall surface behind the radiators, to which the opaque-wall U value is applied (Section 2.4.3).

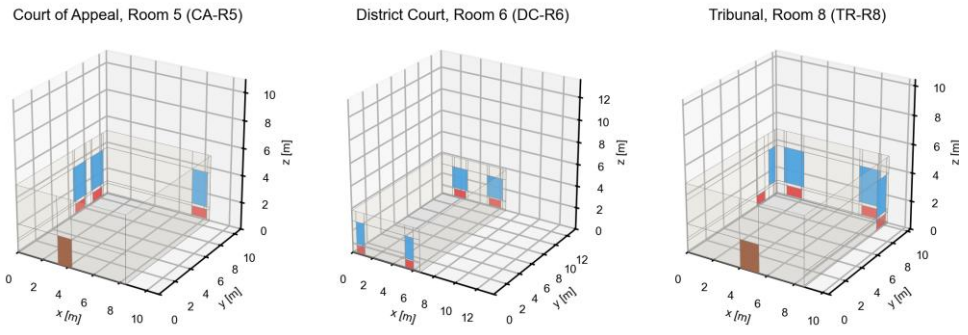


Figure 1. Three-dimensional models of the simulated courtrooms (blue: windows; red: radiators; brown: doors).

2.2. Infrared Thermography

We surveyed the façades of the Court of Appeal and Tribunal building with an infrared camera (FLIR E6xt, Teledyne FLIR LLC, Wilsonville, OR, USA, 240 × 180 pixels) on 8 February 2025 between 06:13 and 06:24, before sunrise, with an outdoor temperature of −4 °C and a relative humidity of 77%; at the same time the indoor air in CA-R5 was at 22.6 °C. We recalculated the apparent temperatures from the raw radiometric data with an emissivity of 0.90 and with reflected and atmospheric temperatures equal to the outdoor air temperature. Wind and sky radiation affect the exterior surface temperature, so we used thermography qualitatively [33–35]: we separated windows and opaque zones by temperature percentiles and compared them through the exterior surface temperature factor $f_e = (T_{se} - T_e)/(T_i - T_e)$, which grows with the local heat flux.

2.3. Numerical Model

We solved the steady, buoyancy-driven flow with buoyantSimpleFoam of OpenFOAM v2512 [11] and the Boussinesq approximation:

$$\nabla \cdot \boldsymbol{U} = 0 \tag{1a}$$

$$\nabla \cdot (\boldsymbol{U}\boldsymbol{U}) = -\frac{1}{\rho_0}\nabla p_{rgh} - \boldsymbol{g} \cdot \boldsymbol{r}\,\nabla\frac{\rho}{\rho_0} + \nabla \cdot [(\nu + \nu_t)(\nabla \boldsymbol{U} + \nabla \boldsymbol{U}^T)] \tag{2b}$$

$$\nabla \cdot (\boldsymbol{U}h) = \nabla \cdot [(\alpha + \alpha_t)\nabla h] + \frac{S_h}{\rho_0}, \qquad \rho = \rho_0[1 - \beta(T - T_0)] \tag{3}$$

where **U** is the mean velocity; ϱ_0 = 1.2 kg/m³ the air density at T_0 = 294.15 K (21 °C); β = $3.4 \cdot 10^{-3}$ K^{-1}; **g** the gravitational acceleration and **r** the position vector; $p_{rgh} = p - \varrho\,\mathbf{g}\cdot\mathbf{r}$ the pressure without its hydrostatic part; $\nu = 1.5 \cdot 10^{-5}$ m²/s and $\nu_t = C_\mu k^2/\varepsilon$ (C_μ = 0.09) the molecular and turbulent kinematic viscosities; $h = c_p T$ the sensible enthalpy (c_p = 1005 J/(kg K)); $\alpha = \nu/\mathrm{Pr}$ and $\alpha_t = \nu_t/\mathrm{Pr}_t$ the thermal diffusivities (Pr = 0.71, Pr_t = 0.85); and S_h the volumetric heat source of radiators and occupants (W/m³). In Equation (1b), $\nabla\varrho/\varrho 0 = -\beta\nabla T$. Air is transparent to radiation, which acts only through Equation (4).

Choice of turbulence model. The flow is slow and buoyancy-driven: the occupied-zone mean speed is 0.06–0.11 m/s and the peak speed along the cold walls 0.3–0.6 m/s. The largest surface-to-air difference of the existing state is about 15–18 K (inner glazing of DC-R6 at 8.9 °C on average and 5.4 °C at its coldest, against 23.8 °C air), so $\beta\Delta T \approx 0.06$ and the Boussinesq approximation holds. The Rayleigh number based on room height is of the order of 10^{11} and the Reynolds number 10^4–10^5, so the wall layers and radiator plumes are turbulent and the room core weakly turbulent. We used steady RANS with the standard k–ε model and wall functions [36] for three reasons: it is the most widely used model for room airflow, with documented behaviour in buoyant indoor flows [22,23,25]; it is cheap enough for nine scenario cases and the sensitivity runs; and a steady solution answers our question on mean occupied-zone conditions. Large-eddy simulation resolves more of the flow, but RANS remains accepted for indoor applications [24]. The standard k–ε model assumes fully turbulent flow and depends on the near-wall treatment, and the ranking of RANS models depends on the flow case [25] and on the cold-window boundary layer [26]. We therefore repeated CA-R5 and DC-R6 (S0) with the realizable k–ε, RNG k–ε and k–ω SST models, with buoyancy production in the k–ε equations and, in CA-R5, with the standard thermal wall function, and report the spread as model-form uncertainty (Section 3.5).

Schemes and wall treatment. We discretised the convective terms of momentum and energy with a bounded second-order linear-upwind scheme and those of the turbulence quantities with first-order upwind. At walls we used high-Reynolds-number wall functions (nutkWallFunction, epsilonWallFunction, kqRWallFunction) and the thermal wall function of Jayatilleke. The first cell centre lies 0.075 m from the wall on the 0.15 m meshes. In the nine cases of the revised model (M1), the area-weighted mean y+ over all walls was 76–116, with a range of 23–314 and at most 0.6% of the wall area below y+ = 30; the windows had the highest values (area-weighted means 96–178). The y+ scales with cell size (area-weighted means 68, 105 and 139 for 0.10, 0.15 and 0.20 m cells in CA-R5, first model), so the log-law branch applies on all meshes but no mesh resolves the viscous sublayer.

Limits of wall functions. A y+ above 30 shows that the wall functions are used within their range of validity, not that they are accurate. They are calibrated on forced, near-equilibrium boundary layers, whereas the velocity of a natural-convection layer along a vertical wall peaks within millimetres to centimetres of the wall, below the first cell. The

wall heat flux and the near-wall velocity therefore carry an uncertainty that mesh refinement cannot remove within the wall-function approach. It affects the convective transfer at glazing, walls and radiators and the ankle-level velocity and draught rate near the façade, whereas the mean temperature and PMV depend mainly on the global energy balance. We bound the effect by the turbulence-model spread (Section 3.5) and by a comparison with the downdraught correlation of Heiselberg [3] (Section 3.6), and we read near-façade velocities and draught rates as indicative.

Mesh quality. All meshes are pure hexahedral grids of rectangular cells. checkMesh reports a maximum non-orthogonality of 0°, a maximum skewness of the order of 10^{-13} and a maximum aspect ratio of 1.03 for all meshes (0.075–0.20 m), with no failed check. The Fluent-equivalent orthogonal quality is 1.0 and the equiangle skewness 0.0 (derived from the cell geometry; Table S3), so mesh quality does not limit the solution.

2.4. Boundary Conditions, Radiation and Retrofit Scenarios

We solved two versions of the thermal boundary conditions: the reference model M0 of the first submission and the revised model M1, which adds surface radiation and couples the surfaces to the envelope resistance. M0 appears only in Section 3.4; all other results refer to M1.

2.4.1. Reference Model M0: Prescribed Surface Temperatures

In M0, a one-dimensional steady balance at the design condition gave the inner surface temperatures of exterior walls and windows,

$$T_{si} = T_{set} - U\,R_{si}\,(T_{set} - T_e) \tag{4}$$

where U is the thermal transmittance (W/(m² K)), R_{si} = 0.13 m² K/W the conventional inner surface resistance [37], T_{set} = 21 °C the indoor set-point and T_e = −18 °C the outdoor design temperature for Iași [38]. We imposed T_{si} and kept the interior walls, floor, ceiling and doors at T_{set}; such prescribed-temperature conditions are common in CFD of radiator-heated rooms [4].

M0 has two inconsistencies. First, $1/R_{si}$ = 7.7 W/(m² K) combines convection and radiation (about 5 W/(m² K) for ε = 0.9), but M0 has no radiation model, so the exchange was purely convective. Second, Equation (3) assumes a room-side temperature of T_{set}, whereas the computed occupied-zone air was 23–24 °C, so the heat leaving through the envelope depends on the wall functions instead of the U-value. Both bias the air and radiant temperatures of M0.

2.4.2. Revised Model M1: Radiation and Coupled Envelope

Radiation. We solved the radiative exchange with the grey, diffuse surface-to-surface model of OpenFOAM (viewFactor, face agglomeration, solved at every iteration) and non-participating air, the usual assumption indoors [39]. The emissivity is 0.90 for walls, floor, ceiling, doors and radiators and 0.84 for the glazing. It was used in all M1 cases and gives the mean radiant temperature (Section 2.5).

Coupled envelope. Instead of fixing T_{si}, we coupled each element to the ambient on its other side through its resistance: at every boundary face, the flux that leaves the room by convection and radiation equals the flux through the element,

$$q_c + q_r = \frac{T_s - T_a}{R_l + \frac{1}{h_o}} \tag{5}$$

where q_c is the convective flux from the first cell given by the thermal wall function, q_r the net radiative flux (both positive towards the wall, W/m²), T_s the unknown room-side surface temperature, T_a the temperature on the other side, h_o the heat-transfer coefficient

there and R_l the resistance of the element, one conductive layer without thermal mass because the solution is steady:

$$R_l = \begin{cases} \frac{1}{U} - R_{si} - R_{se}, \text{exterior walls and windows}, T_a = T_e, h_o = \frac{1}{R_{se}} \\ \frac{1}{U_{int}} - 2R_{si}, \text{interior elements}, T_a = T_{set}, h_o = \frac{1}{R_{si}} \end{cases} \quad (6)$$

with R_{se} = 0.04 m² K/W [37]. For exterior elements $R_l + 1/h_o = 1/U - R_{si}$, so the model resolves the inner film itself and keeps the rest of the U-value in the element; the wall behind each radiator is an exterior wall. Interior elements adjoin rooms at T_{set} with U_{int} = 1.8 W/(m² K) (walls, doors) and 2.0 W/(m² K) (floor, ceiling), assumed values typical of masonry partitions and concrete slabs, since no survey of the interior elements was available. Surface and air temperatures and heat flows to neighbours are the results. We tested neighbours at 23 °C (case CL-N23) and, in M0, the reference temperature of Equation (3) at 23 and 24 °C (cases CL-23 and CL-24) (Section 3.4).

2.4.3. Heating Power, Occupants and Radiators

The design radiator output follows from the transmission loss and the occupant gains,

$$Q_{rad} = \max\{0, Q_{trans} - Q_{occ}\}, Q_{trans} = \left(\sum U_w A_w + \sum U_g A_g\right)(T_{set} - T_e) \quad (7)$$

where U_w, A_w and U_g, A_g are the transmittances and areas of exterior walls and windows and Q_{occ} = 900 W. Q_{rad} is shared among the radiators by area and is the same in M0 and M1. The areas are those of the model geometry, which include the wall behind the radiators, so Equation (6) reproduces Table 2 within its rounding; Table 1 now lists these model areas. The 12 occupants (75 W sensible heat each) form a uniform convective volumetric source in the occupied zone (0–1.2 m above the floor, more than 0.6 m from the walls, outside the court platform).

Table 2. Thermal transmittances, M0 inner surface temperatures (Equation (3)) and design heat loads (Equation (6)).

Scenario	Building	U_{wall}/U_{window} [W/(m²K)]	$T_{si,wall}/T_{si,window}$ (M0) [°C]	CA-R5 Q_{trans}/Q_{rad} [W]	TR-R8 Q_{trans}/Q_{rad} [W]	DC-R6 Q_{trans}/Q_{rad} [W]
S0	CA, TR	0.40/1.60	19.0/12.9	2017/1117	2816/1916	–
S0	DC	1.25/2.60	14.7/7.8	–	–	2970/2070
S1	CA, TR	0.40/0.90	19.0/16.4	1704/804	2461/1561	–
S1	DC	1.25/0.90	14.7/16.4	–	–	2350/1450
S2	CA, TR	0.25/0.90	19.7/16.4	1216/316	1709/809	–
S2	DC	0.25/0.90	19.7/16.4	–	–	733/0

CA-R5: 83.38/11.48; TR-R8: 128.50/13.00; DC-R6: 41.46/9.36 ($A_{wall,ext}/A_{window}$, m²). –: not applicable (the row refers to the other building).

Radiator representation. Each radiator is a volumetric heat source in the air layer in front of its outline,

$$S_{h,i} = \frac{Q_{rad,i}}{V_i} \quad (8)$$

where $Q_{rad,i}$ is the share of radiator i and V_i the volume of the cells that contain the source. Volumetric sources are common in room CFD with heaters [40] and need no radiator geometry or water temperature, which the survey did not record. The layer described as 0.1 m thick in the first submission was in fact one cell (0.15 m on the 0.15 m mesh), because the source fills the cells whose centres lie in a box of nominal depth 0.1 m. In M1 the box

depth is 0.15 m: one cell layer on the 0.15 and 0.10 m meshes and two on the 0.075 m mesh, with the same total output. The source delivers all heat by convection, whereas a panel radiator emits 11–30% by radiation [41,42], and it gives no surface temperature. We tested two variants (Section 3.5): a source two cell layers deep (RAD-V) and the radiator outline as an isothermal heated surface (RAD-S), whose temperature we adjusted until the surface delivered the design output and whose radiative fraction is a result. An imposed uniform heat flux on the radiator surface was also tried but was ill-posed on this mesh with wall functions (local surface temperatures of several hundred kelvin in stagnant cells), so it is not used. The two variants bound real panel radiators: the volumetric source is purely convective and the isothermal flat surface mostly radiative. Surface heat-transfer coefficients on radiators can differ strongly from standard values [43].

2.4.4. Ventilation Cases

The base cases have no ventilation. We added ventilation cases for DC-R6 (S2) and CA-R5 (S0), with the flow of category II of EN 16798-1 [44],

$$\dot{V} = n_{\mathrm{p}} q_{\mathrm{p}} + A_{\mathrm{f}} q_{\mathrm{A}} \tag{9}$$

with n_p = 12 persons, q_p = 7 L/s per person, q_A = 0.7 L/s per m² and the floor area A_f of Table 1, which gives 146.5 L/s (DC-R6) and 148.2 L/s (CA-R5), 1.2–1.5 air changes per hour. Heating this flow from T_e to T_{set} needs

$$Q_{\mathrm{vent}} = \rho\, c_{\mathrm{p}} \dot{V} (1 - \eta)(T_{\mathrm{set}} - T_{\mathrm{e}}) \tag{10}$$

which is 6.9–7.0 kW without recovery and about 1.7 kW with a sensible recovery efficiency η = 0.75, when the supply air leaves the exchanger at

$$T_{\mathrm{sup}} = T_{\mathrm{e}} + \eta (T_{\mathrm{ex}} - T_{\mathrm{e}}) \tag{11}$$

that is 12 °C for an assumed extract temperature T_{ex} = 22 °C. The supply is a mixing jet of 1.65–1.72 m/s from a 0.30 × 0.30 m grille on the interior east wall, with its top about 0.3 m below the ceiling, and the extract on the same wall; the inlet turbulence follows from a mixing length of 0.03 m (10% of the grille size). We ran three supply temperatures. In case V-a, a central coil heats the supply air to T_{set} = 21 °C, so the radiators keep the output of Table 2. In case V-b, the supply air enters at T_{sup} = 12 °C without reheating, and in case V-c it is reheated to 18 °C; in both, the radiators cover the remaining sensible load,

$$Q_{\mathrm{rad}}^{\mathrm{V\text{-}b,c}} = \max\{0, Q_{\mathrm{trans}} + \rho\, c_{\mathrm{p}} \dot{V} (T_{\mathrm{set}} - T_{\mathrm{sup}}) - Q_{\mathrm{occ}}\} \tag{12}$$

where the clipping applies to the sum, not to the Table 2 value. Evaluated with the simulated mass flow, this gives 2726 W (V-b) and 1670 W (V-c) for CA-R5 (S0) and 1423 W (V-b) and 379 W (V-c) for DC-R6 (S2). The CFD uses dry air, without infiltration.

2.4.5. Retrofit Scenarios

We analysed the existing state (S0), window replacement with triple low-e glazing (S1) and window replacement with external wall insulation to a nearly zero-energy level (S2) (Table 2). No envelope survey was available; the transmittances are typical values for the two construction periods and current requirements [38]. The T_{si} columns of Table 2 are the prescribed M0 temperatures; in M1 they are results (Section 3.4).

2.5. Comfort Indicators and Criteria

We evaluated thermal comfort with the PMV–PPD model of ISO 7730 [45] in every cell for a clothing insulation of 1.0 clo, a metabolic rate of 1.2 met (seated, light activity) and 35% RH. The RH measured during occupied hours was lower (24–29%), but at these

temperatures the difference lowers the PMV by less than 0.1. The mean radiant temperature (T_{mrt}) is the area-weighted mean temperature of the room surfaces in M0 and the radiation-based value in M1 (Section 2.4.2); the operative temperature is $T_{op} = (T_{air,occ} + T_{mrt})/2$ and the PPD follows from the PMV. Two indicators describe local discomfort: the draught rate DR [45,46] and the vertical air temperature difference between the head (1.1 m) and ankle (0.1 m) height of seated occupants; ISO 7730 and EN 16798-1 recommend a difference below 3 K and a draught rate below 20% for category B/II [44,45]. We calculated DR in post-processing with the ISO 7730 expression, $DR = (34 - T)\,(v - 0.05)^{0.62}\,(0.37\,v\,Tu + 3.14)$, where T is the local air temperature in °C, v the local speed clipped to 0.05–0.5 m/s, and Tu the turbulence intensity in %, $Tu = 100\,\sqrt{(2k/3)}/\max(v, 0.05)$ from the turbulent kinetic energy k of the RANS solution and limited to 10–60%; DR was capped at 100% [45]. As a sensitivity test, we set Tu = 40%. The comfort function object of OpenFOAM v2512 that we used in the first submission evaluates the turbulence intensity with an integer division, which sets it, and so the turbulence term of DR, to zero; the DR values of the submitted version are therefore replaced by the values given here. Because RANS k is only a proxy for the turbulence of the real flow near the façade, DR is an indicative quantity (Section 3.9). We computed the indicators from the cell values with Python 3.12 (PyVista) and visualised the flow fields with Tecplot 360 EX 2025 R1.

2.6. Verification and Validation

Verification asks whether the equations are solved correctly; validation asks whether the model represents the physical room and needs measurements [30,31].

Iterative convergence. The existing-state cases (S0) ran for 6000 SIMPLE iterations with the fields averaged over iterations 4000–6000 to remove the oscillation of the weakly unsteady flow. The retrofit and sensitivity cases started from the converged S0 field of the same room, ran for 8000 iterations with under-relaxation 0.3 on the wall temperatures and were averaged over iterations 6000–8000. We required a global energy-balance error below 5% and a drift of the occupied-zone air temperature below 0.05 K over the last 1000 iterations; a case that missed either limit was extended by 2000 iterations. The nine scenario cases (Section 3.7) reached balance errors of 0.04–1.4% and drifts of at most 0.02 K (Table S2).

Mesh verification. We solved the existing state of CA-R5 and DC-R6 on meshes of 0.15, 0.10 and 0.075 m and estimated the discretisation error with the grid convergence index (GCI) procedure [32] (Section 3.2).

Code-to-code comparison. We solved the nine cases with Ansys Fluent 2025 R2 on the same meshes (exported with foamMeshToFluent), with the same boundary conditions, sources and Boussinesq parameters, standard k–ε with standard wall functions, SIMPLE, PRESTO! pressure interpolation and second-order upwind for momentum and energy, for 10,000 iterations averaged over the last 2000. Radiation used Fluent's surface-to-surface (S2S) model with view factors from ray tracing, one face per cluster and an update every 10 iterations; the existing state of CA-R5 and DC-R6 was also solved on the 0.075 m meshes, starting from the interpolated 0.15 m solution (4000 and 6000 iterations, averaged over the last 2000). This is verification: both codes solve the same model, so their difference measures implementation and discretisation effects and cross-checks the view-factor radiation of OpenFOAM.

Validation V1: downdraught correlation. We simulated the CA-R5 room without heat sources at an outdoor temperature of −10 °C so that the glazing (height H = 2.55 m) was 7.6 K colder than the occupied-zone air (18.9 °C), inside the range of the correlation of Heiselberg [3]. With the mesh, turbulence model and wall treatment of the courtroom cases (meshes 0.15 and 0.10 m), we compared the velocity of the cold layer near the floor at 0.5–4.0 m from the façade with the correlation. The test addresses the velocity scale of

the downdraught. The correlation has its own scatter and serves as a benchmark, not a measurement.

Validation V2: measured air temperatures. The monitoring campaign of winter 2025 recorded the air temperature with one logger per room (Testo 174H, Testo SE & Co. KGaA, Titisee-Neustadt, Germany, ±0.5 K) at 1.1–1.5 m height. We used unoccupied, quasi-steady night periods (Section 3.6), setting the outdoor temperature to the measured mean, removing the occupant source and holding the neighbouring rooms at the measured room temperature. We calibrated the radiator output once per room, on 8 February, so that the simulated temperature at the logger matched the measurement (the logger position was not recorded, so we used the mean of the room-centre column at 1.1, 1.3 and 1.5 m), and checked the calibration with a separate run at the calibrated output. For CA-R5 we then predicted 23 February and 15–16 March without further adjustment, keeping the calibrated output constant (uncontrolled radiators); an output scaled with the outdoor temperature is given as a sensitivity. For the predictions the neighbouring rooms were first kept at the calibration temperature; if the simulated room then differed from it by more than 0.3 K, they were set once to the simulated room temperature, a rule fixed before the runs. We report bias, mean absolute error (MAE) and root-mean-square error (RMSE) at the logger.

V1 and V2 test the velocity scale and one air temperature per room. They do not test the velocity field, the vertical profile or the draught rate, for which no measurements exist, and agreement at one point does not exclude compensating errors.

3. Results and Discussion

3.1. Thermographic Survey

At the Court of Appeal and Tribunal building (Figure 2), the windows of the courtroom floors were the warmest elements of the envelope. Their median apparent temperature was 1.7 °C (f_e = 0.21), against −1.8 °C (f_e = 0.09) on the opaque parts of the same façade, a local heat flux more than twice as high. On the panel-clad façade, the aluminium panels stayed close to the outdoor air temperature (median −3.1 °C), as expected for a ventilated cladding decoupled from the insulation layer, while the vertical panel joints and the glazed ground floor appeared as warm lines and bands (95th percentile of the joints −0.1 °C, glazing 2.8 °C). The lower emissivity of glass and sky reflection distort its apparent temperatures, so we did not use them quantitatively. The survey points to the glazing as the weakest element of the envelope of the recent building, which supports the window-replacement scenario.

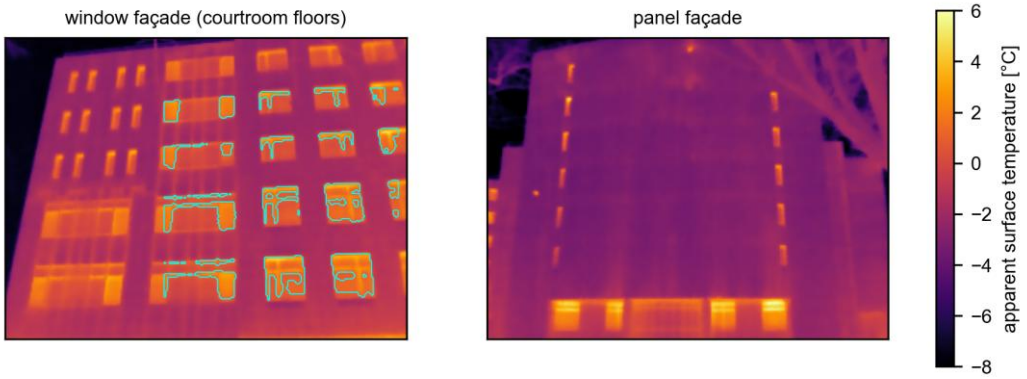


Figure 2. Thermograms of the Court of Appeal and Tribunal building, 8 February 2025, 06:15–06:22 (T_e = −4 °C, ε = 0.90): window façade of the courtroom floors (contour: window zones) and panel-clad façade.

3.2. Mesh Sensitivity and Grid Convergence

3.2.1. Procedure and Acceptance Criteria

All meshes are uniform hexahedral grids of cell edge h. We refined the CA-R5 (S0) mesh from 0.20 to 0.15, 0.10 and 0.075 m (ratios 1.33, 1.5, 1.33); the 0.20 m mesh was solved only with M0. For solutions φ_1, φ_2, φ_3 on the fine, medium and coarse mesh, we followed Celik et al. [32] (Equations (S1) and (S2)), and the grid convergence index of the fine grid is

$$\mathrm{GCI}_{\mathrm{fine}}^{21} = \frac{F_s \left| \frac{\varphi_1 - \varphi_2}{\varphi_1} \right|}{r_{21}^{p} - 1} \tag{13}$$

with r_{21} = h2/h1, the apparent order p and F_s = 1.25 for three grids [32]; $U_{num} = \mathrm{GCI} \cdot |\varphi_1|$ is the absolute uncertainty. The ratio $R = (\varphi_2 - \varphi_1)/(\varphi_3 - \varphi_2)$ classifies the convergence: $0 < R < 1$ is monotonic, $R < 0$ oscillatory, $R > 1$ outside the asymptotic range; in the last two cases, we report the range of the three solutions and no GCI [32]. We analysed T_{room}, T_{occ}, $\Delta T_{1.1–0.1}$, the mean air speed u_{occ}, the PMV and the mean draught rate DR.

We set two acceptance criteria for the 0.15 m mesh before the runs: a discretisation error of T_{occ} on that mesh, $|\varphi_3 - \varphi_{ext}|$, of at most 0.5 K (the logger accuracy), and, for $\Delta T_{1.1–0.1}$, u_{occ} and DR, monotonic convergence with GCI ≤ 20% or else the range of the three solutions as an uncertainty band. These thresholds are our own choice; [32] defines the procedure but does not specify a threshold.

The apparent order p is approximate, because the schemes mix second- and first-order terms, and the GCI does not separate the discretisation error from the dependence of the wall functions on y+. Voxelisation changes the areas slightly with h, so Q_{rad} was kept at its Table 2 value on all meshes (Q_{trans} of each mesh in Table S1).

3.2.2. Original Model M0 (0.20, 0.15 and 0.10 m)

On the M0 meshes (Table 3), the occupied-zone air temperature converged monotonically (23.16, 23.05 and 22.97 °C; GCI 0.45%, U_{num} = 0.10 K, Table S1), whereas the head–ankle difference (1.20, 1.15 and 0.79 K), the draught rate and the PMV were outside the asymptotic range (R = 8.1, 2.8 and 1.4), and the finest solution still drifted. We therefore repeated the analysis for M1 with averaged fields and a finer mesh.

Table 3. Mesh and code sensitivity of the air temperature and speed (CA-R5, S0, model M0). DR is calculated as described in Section 2.5 (the submitted version gave 4.6, 5.0 and 5.9%).

Code	Cell Size [m]	Cells	T_{room} [°C]	T_{occ} [°C]	$\Delta T_{1.1–0.1}$ [K]	u_{occ} [m/s]	$u_{occ,P95}$ [m/s]	PMV	DR [%]
OpenFOAM	0.2	56,700	23.46	23.16	1.20	0.10	0.22	−0.04	6.7
OpenFOAM	0.15	134,904	23.30	23.05	1.15	0.10	0.20	−0.05	7.2
OpenFOAM	0.1	448,644	23.16	22.97	0.79	0.12	0.22	−0.08	8.5
Fluent	0.15	134,904	22.89	22.77	0.71	0.12	0.23	–	–

–: not evaluated for the Fluent case.

3.2.3. Revised Model M1 (0.15, 0.10 and 0.075 m)

For M1 we solved CA-R5 (S0) on meshes of 0.15, 0.10 and 0.075 m (134,904, 448,644 and 1,055,600 cells) with averaged fields (Section 2.6). The 0.10 m case converged slowly with the wall-temperature under-relaxation and needed 10,000 iterations; its energy balance closed within 1.9% and the drift of T_{occ} over the last 1000 iterations was 0.06 K, slightly above our limit, which we accept as part of its uncertainty (Table S2).

Table 4 gives the results. The occupied-zone air temperature converged monotonically (22.89, 22.90 and 23.17 °C on the 0.075, 0.10 and 0.15 m meshes; R = 0.00): the 0.10 and 0.075 m solutions coincide, and the 0.15 m mesh overestimates the extrapolated value by 0.27 K. The head–ankle difference also converged monotonically but slowly (0.74, 0.88 and 1.32 K; R = 0.31, p = 2.4, φ_{ext} = 0.59 K, GCI of the fine grid 24%), so the 0.15 m mesh overestimates it by about 0.7 K. The peak near-façade speed rose with refinement (0.41, 0.49 and 0.52 m/s; φ_{ext} = 0.56 m/s), so the 0.15 m mesh underestimates it by about a quarter, in line with V1 (Section 3.6). The occupied-zone speed (0.087–0.094 m/s) and the mean DR (5.6–6.5%) were not in the asymptotic range (R = 1.8 and 1.1); we report their ranges. In DC-R6, solved on the 0.15 and 0.075 m meshes, the refinement lowered T_{occ} by 0.59 K and $\Delta T_{1.1–0.1}$ from 2.09 to 1.22 K and raised the peak near-façade speed from 0.56 to 0.63 m/s, the same trends as in CA-R5.

Table 4. Grid convergence of CA-R5 (S0, model M1) on meshes of 0.15, 0.10 and 0.075 m: solutions φ, convergence ratio R, apparent order p, extrapolated value φ_{ext}, GCI of the fine grid and absolute uncertainty U_{num}. The GCI, p, φ_{ext} and U_{num} are given only for monotonic convergence (0 < R < 1); the T_{room}, PMV and Q_{trans} of each mesh are also in Table S1.

Quantity	φ (0.15 m)	φ (0.10 m)	φ (0.075 m)	R	p	φ_{ext}	GCI_{fine} [%]	U_{num}
T_{room} [°C]	23.46	23.10	23.06	0.13	4.8	23.04	0.09	0.02
T_{occ} [°C]	23.17	22.90	22.89	0.00	14.0	22.89	0.00	0.00
$\Delta T_{1.1–0.1}$ [K]	1.32	0.88	0.74	0.31	2.4	0.59	24.4	0.18
u_{occ} [m/s]	0.087	0.090	0.094	1.81	–	–	–	–
$u_{max,f}$ [m/s]	0.41	0.49	0.52	0.36	2.0	0.56	9.5	0.05
DR [%]	5.6	6.0	6.5	1.07	–	–	–	–
PMV	−0.018	−0.057	−0.062	0.14	4.5	−0.064	4.2	0.003

–: not given, because the convergence is not monotonic.

3.2.4. Mesh Selection

The 0.15 m mesh fulfils the first criterion (error of T_{occ} 0.27 K in CA-R5 and 0.59 K in DC-R6 on two meshes, against the 0.5 K limit) only in CA-R5 and does not fulfil the second, because the head–ankle difference converges slowly and the speed and draught indicators are outside the asymptotic range. We nevertheless report the nine scenario cases and the sensitivity studies on this mesh, which made more than 60 runs affordable, and

attach to its results the mesh component of the uncertainty: 0.3–0.6 K for T_{occ}, 0.6–0.9 K for $\Delta T_{1.1–0.1}$ (which the 0.15 m mesh overestimates) and 0.07–0.11 m/s for the peak near-façade speed (which it underestimates) (Table S6, Section 3.7). We expect the comparison between scenarios to be less affected, because geometry and mesh are the same in all scenarios, but we tested the mesh only in the existing state.

We did not apply local refinement near the façade, because it would vary the first-cell distance where the wall functions need a consistent value and push y+ below 30 (Table S3). Global refinement to 0.075 m tests the wall heat transfer in the whole room (area-weighted mean y+ of 48–131 by surface type in Fluent).

3.3. Code-to-Code Comparison (OpenFOAM vs. Fluent)

We solved all nine cases of the revised model (M1) with both OpenFOAM and Ansys Fluent on the same 0.15 m meshes and the existing state of CA-R5 and DC-R6 also on the 0.075 m meshes (Table 5). This verifies the implementation of one model in two codes; it is not a validation (Section 3.6).

Table 5. OpenFOAM and Ansys Fluent (S2S radiation), model M1: the nine cases on the 0.15 m mesh and the existing state of CA-R5 and DC-R6 on the 0.075 m mesh. Each cell gives the OpenFOAM value and, in brackets, the Fluent value minus the OpenFOAM value. T_{occ} is the occupied-zone air temperature, T_{mrt} the area-weighted mean surface temperature, $T_{op} = (T_{occ} + T_{mrt})/2$ with the same definition in both codes, and Qloss the heat loss through the envelope.

Room	Sc.	h [m]	T_{occ} [°C]	$\Delta T_{1.1–0.1}$ [K]	u_{occ} [m/s]	DR [%]	T_{mrt} [°C]	T_{op} [°C]	Q_{loss} [W]
CA-R5	S0	0.15	23.2 (−0.34)	1.3 (−0.50)	0.09 (+0.01)	5.6 (+1.1)	20.3 (−0.01)	21.7 (−0.18)	2018 (+7)
CA-R5	S1	0.15	23.0 (−0.38)	1.2 (−0.47)	0.09 (+0.02)	5.7 (+1.5)	20.5 (−0.04)	21.8 (−0.21)	1708 (+1)
CA-R5	S2	0.15	22.8 (−0.34)	1.0 (−0.40)	0.11 (+0.01)	7.9 (+1.3)	20.6 (−0.03)	21.7 (−0.19)	1209 (−1)
TR-R8	S0	0.15	23.6 (−0.35)	1.8 (−0.57)	0.06 (+0.01)	3.2 (+0.2)	20.1 (−0.11)	21.9 (−0.23)	2836 (0)
TR-R8	S1	0.15	23.5 (−0.33)	1.7 (−0.56)	0.07 (+0.03)	3.7 (+2.9)	20.3 (−0.12)	21.9 (−0.23)	2481 (−10)
TR-R8	S2	0.15	23.1 (−0.40)	1.2 (−0.48)	0.09 (+0.03)	5.9 (+2.6)	20.5 (−0.05)	21.8 (−0.22)	1714 (+1)
DC-R6	S0	0.15	23.8 (−0.17)	2.1 (−0.64)	0.06 (0.00)	3.0 (−0.1)	19.8 (0.00)	21.8 (−0.09)	3012 (+21)
DC-R6	S1	0.15	23.6 (−0.22)	1.9 (−0.60)	0.07 (+0.01)	3.2 (+0.3)	20.1 (+0.01)	21.8 (−0.11)	2361 (+12)
DC-R6	S2	0.15	23.0 (−0.29)	1.1 (−0.38)	0.07 (+0.03)	3.6 (+2.8)	20.9 (−0.02)	22.0 (−0.16)	730 (0)
CA-R5	S0	0.075	22.9 (−0.15)	0.7 (−0.09)	0.09 (0.00)	6.5 (−0.2)	20.3 (+0.05)	21.6 (−0.05)	2047 (+4)
DC-R6	S0	0.075	23.2 (−0.19)	1.2 (−0.13)	0.07 (−0.01)	3.4 (−0.8)	19.8 (+0.04)	21.5 (−0.07)	3090 (+33)

First model (M0). In the first submission, Fluent gave occupied-zone and room-mean air temperatures 0.28 and 0.41 K lower than OpenFOAM and a better-mixed room ($\Delta T_{1.1–0.1}$ of 0.71 K against 1.15 K; cell-by-cell r = 0.64, RMSE 0.51 K), and neither solution met the residual limits.

Revised model (M1), 0.15 m. Both codes now converge (Section 2.6) and agree on the global heat balance: the envelope heat loss differs by −10 to +21 W (at most 0.7%), the area-weighted mean radiant temperature by −0.12 to +0.01 K and the mean window surface temperature by at most 0.5 K. The air is consistently cooler in Fluent: the occupied-zone air temperature by 0.17–0.40 K, the operative temperature by 0.09–0.23 K and the head–ankle difference by 0.38–0.64 K. The occupied-zone speed agrees within 0.03 m/s. In CA-R5 (S0) the cell-by-cell comparison of the mean temperature fields gives r = 0.80 and RMSE 0.55 K over the room. Both codes rank the scenarios identically: the occupied-zone air temperature falls from S0 to S1 to S2 in every room.

Mesh refinement. On the 0.075 m meshes, the codes converge towards each other: the difference in the head–ankle difference falls to 0.09 K (CA-R5) and 0.13 K (DC-R6), in the occupied-zone air temperature to 0.15 and 0.19 K and in the operative temperature to 0.05 and 0.07 K, while the occupied-zone speed and the mean draught rate agree within

0.01 m/s and 0.8 percentage points. Most of the code-to-code difference on the 0.15 m mesh is therefore discretisation error, not a difference between the models; it is largest for the stratification, which depends on the thin, under-resolved layers near the floor, the windows and the radiators. The local flow near the façade remains code-dependent even on the finer mesh: the peak near-façade speed is 0.08–0.14 m/s lower in Fluent, and the radiator plume rises along the glazing in Fluent but separates from it at about 1 m in OpenFOAM (Figure S2). The thermal wall functions (Jayatilleke in OpenFOAM, the standard function in Fluent) and the pressure–buoyancy treatment differ between the codes and act mainly in these layers; we did not separate them with dedicated runs.

The comparison supports the mean thermal state of the rooms and the ranking of the scenarios. The head–ankle difference and the near-façade velocities carry the largest numerical uncertainty, which we quantify together with the mesh and modelling effects in Section 3.7.

3.4. Effect of Radiation and Coupled Boundary Conditions

We quantify the two inconsistencies of M0 (Section 2.4.1) by comparing M0 and M1 in the existing state (Table 6) and by the cases CL-23 and CL-N23 (Table 7).

Table 6. Occupied-zone indicators of the original model (M0) and the revised model (M1), existing state (S0), 0.15 m mesh. T_{mrt} is the area-weighted mean surface temperature in M0 and the radiation-based value in M1; $T_{si,w}$ is the window surface temperature (prescribed in M0). DR is calculated as described in Section 2.5; the M0 values replace those of the submitted version (5.0, 3.0 and 2.2%).

Room	Model	$T_{air,occ}$ [°C]	T_{mrt} [°C]	T_{op} [°C]	$T_{si,w}$ [°C]	$\Delta T_{1.1–0.1}$ [K]	PMV	DR [%]	$u_{max,f}$ [m/s]
CA-R5	M0	23.1	20.3	21.7	12.9	1.2	−0.05	7.2	0.40
CA-R5	M1	23.2	20.3	21.7	13.0	1.3	−0.02	5.6	0.41
CA-R5	M1 − M0	+0.1	0.0	+0.1	+0.2	+0.2	+0.04	−1.6	+0.01
TR-R8	M0	23.4	20.0	21.7	12.9	1.5	−0.01	4.4	0.42
TR-R8	M1	23.6	20.1	21.9	13.1	1.8	0.03	3.2	0.41
TR-R8	M1 − M0	+0.2	+0.1	+0.2	+0.2	+0.3	+0.05	−1.1	−0.01
DC-R6	M0	23.7	19.8	21.8	7.8	1.8	0.02	3.1	0.54
DC-R6	M1	23.8	19.8	21.8	8.9	2.1	0.02	3.0	0.56
DC-R6	M1 − M0	+0.1	0.0	0.0	+1.1	+0.3	+0.01	−0.2	+0.02

Table 7. Sensitivity of the occupied-zone indicators and of the envelope heat flow to the 21 °C assumption (S0, 0.15 m mesh): M0 with the reference temperature of Equation (3) and of the interior surfaces at 21 (base), 23 (CL-23) and 24 °C (CL-24), and M1 with the neighbouring rooms at 21 (base) and 23 °C (CL-N23). $T_{si,w}$ is the mean window surface temperature; the heat to the interior is the heat flow to the interior surfaces (M0) or to the neighbouring rooms (M1), positive out of the room.

Case	Room	Model	Reference Temperature [°C]	$T_{air,occ}$ [°C]	T_{mrt} [°C]	T_{op} [°C]	$T_{si,w}$ [°C]	Envelope Loss [W]	Heat to Interior [W]
base	CA-R5	M0	T_{set} = 21	23.1	20.3	21.7	12.9	1058	953
CL-23	CA-R5	M0	T_{set} = 23	25.0	22.3	23.7	14.5	1136	908
CL-24	CA-R5	M0	T_{set} = 24	26.0	23.2	24.6	15.3	1087	940
base	DC-R6	M0	T_{set} = 21	23.7	19.8	21.8	7.8	1433	1534
CL-23	DC-R6	M0	T_{set} = 23	25.7	21.8	23.7	9.1	1445	1514
CL-24	DC-R6	M0	T_{set} = 24	26.6	22.8	24.7	9.8	1462	1493
base	CA-R5	M1	neighbours 21	23.2	20.3	21.7	13.0	2018	−2
CL-N23	CA-R5	M1	neighbours 23	25.0	22.2	23.6	14.5	2114	−86

Air and radiant temperature. Figure 3 shows the air temperature and velocity in a vertical section through a window of CA-R5 and DC-R6, in the existing state and after the full retrofit. Between M0 and M1 the occupied-zone air temperature changed by +0.1/+0.2/+0.1 K and the mean radiant temperature by 0.0/+0.1/0.0 K, so the operative temperature changed by +0.1/+0.2/0.0 K and the PMV moved from −0.05, −0.01 and +0.02 to −0.02, +0.03 and +0.02. The simulated window surface temperature was 13.0, 13.1 and 8.9 °C against the prescribed 12.9, 12.9 and 7.8 °C. The local mean radiant temperature at 9 points of the occupied zone was 19.4–20.9 °C, so the area-weighted value hides a spread of 1.0–1.5 K between the façade and rear seats (Figure 4). The radiant temperature asymmetry towards the windows at the first row was 1.6–5.8 K; asymmetry is a local discomfort parameter of its own [28].

Heat balance. In M0, 37–52% of the heat input left by convection to interior surfaces held at 21 °C, and only the rest left through the envelope. In M1 the heat leaves through the windows (29–35%) and the exterior walls (65–72%), while the net exchange with the neighbouring rooms is −2.0 to −0.1% of the input and the global imbalance at most 1.4% (Table S4). M1 confirms that the 21 °C condition of M0 turned the interior surfaces into heat sinks that absorbed a large part of the radiator output.

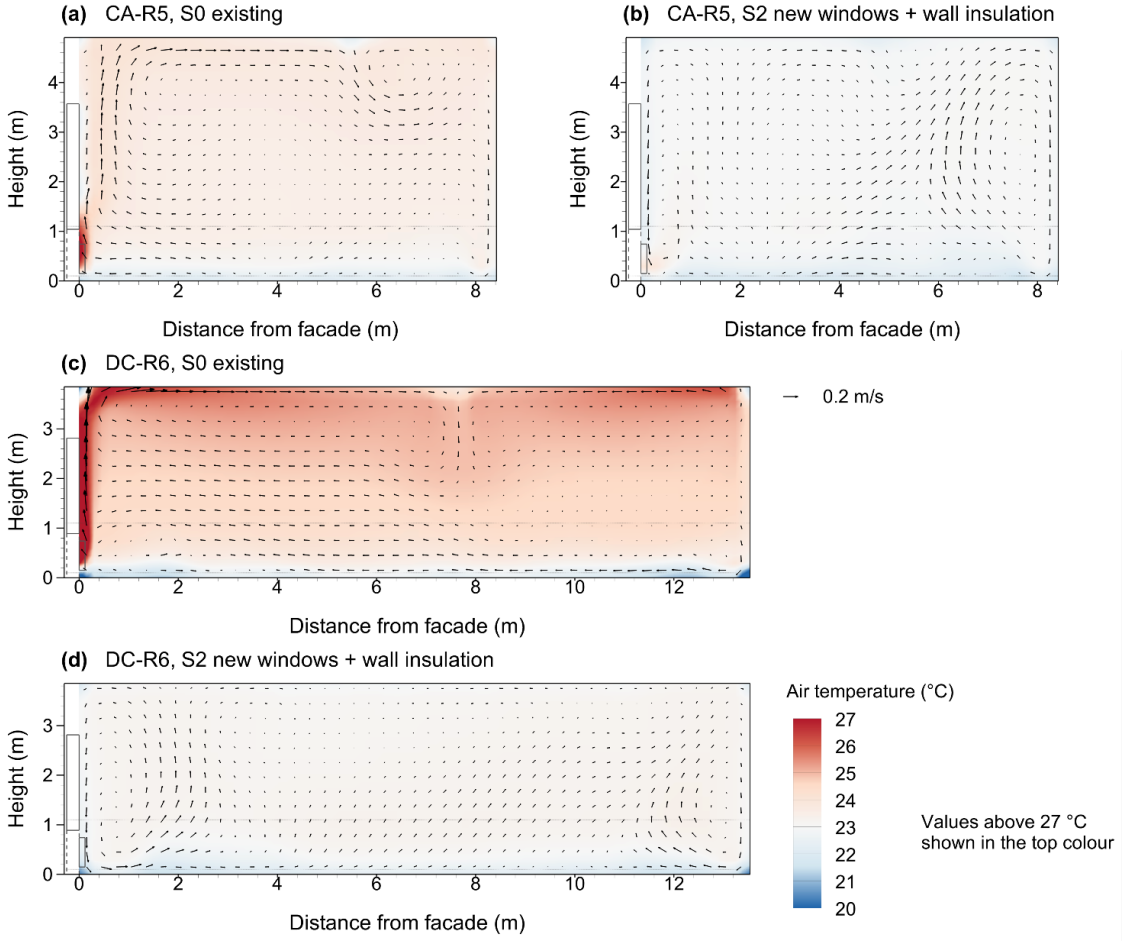


Figure 3. Air temperature and in-plane velocity vectors in vertical sections perpendicular to the main façade through a window (model M1, OpenFOAM, 0.15 m mesh, time-averaged fields): (**a**) CA-R5, S0; (**b**) CA-R5, S2; (**c**) DC-R6, S0; (**d**) DC-R6, S2. The façade is at a distance of 0 m. The reference vector is 0.2 m/s; the colour scale is common to all panels, and values above 27 °C are shown in the top colour. Thin lines: window, parapet, radiator and the heights 0.1 and 1.1 m.

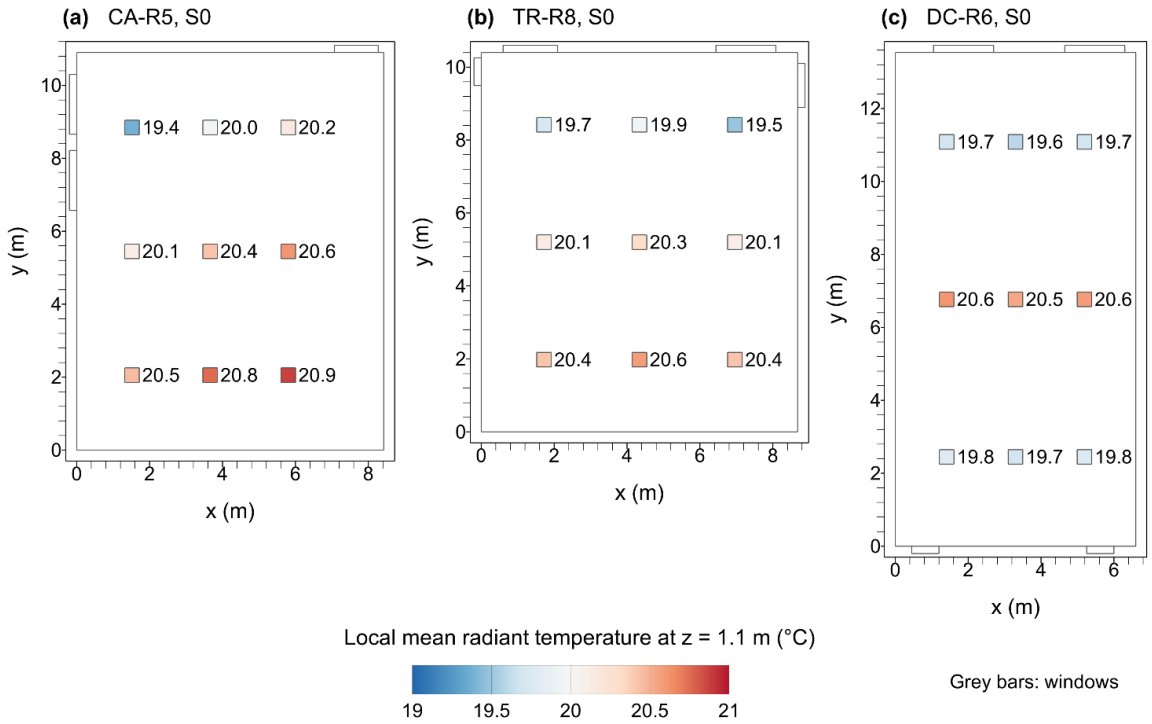


Figure 4. Local mean radiant temperature at nine points 1.1 m above the floor in the existing state (S0, model M1, 0.15 m mesh): (**a**) CA-R5, (**b**) TR-R8, (**c**) DC-R6 (plan views; grey bars: windows).

Sensitivity to the 21 °C assumption. In M0, raising the reference temperature of Equation (3) and of the interior surfaces from 21 to 23 and 24 °C raised the occupied-zone air temperature almost one to one, by 2.0 and 3.0 K in CA-R5 and 2.0 and 2.9 K in DC-R6, and the window surface temperature by 1.3–2.4 K (CL-23, CL-24; Table 7). In M1, neighbouring rooms at 23 °C instead of 21 °C raised the occupied-zone air temperature of CA-R5 by 1.9 K and raised the small heat gain from the neighbours from 2 to 86 W, while the envelope loss rose by 5% (CL-N23). In both models the absolute air temperature follows the temperature assumed for the adjacent rooms, which is therefore one of the largest uncertainties of the study; the excess of the room air over the adjacent rooms (about 2.2 K in M1 at the design output) is the more robust quantity.

Radiation and the coupling changed the occupied-zone air temperature by only 0.1–0.2 K, so the air stayed 2.2–2.8 K above 21 °C. With the interior boundary at 21 °C, this excess results from the radiator sizing of Equation (6) and the occupant gains, not from the radiation treatment. The calibration of V2 (Section 3.6) points the same way: the measured unoccupied temperatures needed only about 55% of the transmission loss computed for that night.

From S0 to S2, the occupied-zone air temperature fell in M0 by 0.4, 0.5 and 1.0 K and the mean radiant temperature rose by 0.3, 0.4 and 0.9 K (CA-R5, TR-R8, DC-R6); in M1, the changes are −0.4, −0.5 and −0.8 and +0.3, +0.4 and +1.1. The ranking of the scenarios is the same in both models.

3.5. Sensitivity to the Turbulence Model and the Radiator Representation

Table 8 gathers the sensitivity runs of M1 for the existing state of CA-R5 and DC-R6: the standard k–ε model of the reference cases with and without buoyancy production of turbulence, the realizable and RNG k–ε models, the k–ω SST model, the standard instead of the Jayatilleke thermal wall function (CA-R5), a radiator source two cell layers deep (RAD-V) and the radiator as an isothermal heated surface (RAD-S).

Table 8. Sensitivity of the indicators to the turbulence model, the wall treatment and the radiator representation (model M1, S0, 0.15 m mesh; reference: standard k–ε, one-layer source). $DR_{max,1}$ is the maximum ankle-level draught rate in the first row of seats. $T_{s,rad}$ and f_r are the surface temperature and the radiative fraction of the radiator in RAD-S.

Room	Variant	$T_{air,occ}$ [°C]	$\Delta T_{1.1-0.1}$ [K]	u_{occ} [m/s]	$u_{max,f}$ [m/s]	DR [%]	$DR_{max,1}$ [%]	$T_{s,rad}$ [°C]	f_r [%]
CA-R5	reference (standard k–ε)	23.17	1.32	0.09	0.41	5.6	24.7	–	–
CA-R5	standard thermal wall function	23.39	1.40	0.09	0.43	5.5	24.6	–	–
CA-R5	standard k–ε with buoyancy production	23.17	1.72	0.09	0.41	5.8	23.7	–	–
CA-R5	realizable k–ε	23.18	1.35	0.09	0.45	5.6	25.5	–	–
CA-R5	RNG k–ε	23.36	1.61	0.08	0.42	4.6	24.8	–	–
CA-R5	k–ω SST	23.57	2.12	0.06	0.45	2.2	24.1	–	–
CA-R5	RAD-V (two layers)	23.24	1.32	0.10	0.41	6.4	26.5	–	–
CA-R5	RAD-S (isothermal)	22.38	0.90	0.11	0.31	8.4	25.2	81.9	78
DC-R6	reference (standard k–ε)	23.76	2.09	0.06	0.56	3.0	28.1	–	–
DC-R6	standard k–ε with buoyancy production	23.72	3.20	0.05	0.53	1.6	26.5	–	–
DC-R6	realizable k–ε	24.05	2.25	0.06	0.60	2.3	29.0	–	–
DC-R6	RNG k–ε	24.13	2.59	0.05	0.56	1.6	25.9	–	–
DC-R6	k–ω SST	24.02	3.13	0.04	0.52	1.1	24.9	–	–
DC-R6	RAD-V (two layers)	23.84	2.06	0.06	0.57	2.9	29.7	–	–
DC-R6	RAD-S (isothermal)	22.25	1.06	0.07	0.45	3.5	27.8	115.5	84

–: not applicable (given only for RAD-S).

Turbulence model and wall treatment. The occupied-zone air temperature varied by 0.40 K (CA-R5) and 0.41 K (DC-R6) across the variants and the occupied-zone speed by at most 0.04 m/s. The head–ankle difference was the most sensitive indicator: 1.32–2.12 K in CA-R5 and 2.09–3.20 K in DC-R6, highest with k–ω SST and with buoyancy production in the k–ε equations. Buoyancy production removes turbulent energy in the stably stratified layers and so reduces the mixing; the lower mixing of k–ω SST in these layers is a model difference that we did not analyse further. The mean draught rate broadly followed the opposite trend (CA-R5 2.2–5.8%, DC-R6 1.1–3.0%): the variants with more stratification predicted less turbulence and therefore less draught. The peak near-façade speed (0.41–0.45 and 0.52–0.60 m/s) and the maximum draught rate at the ankles of the first row (24–26% and 25–29%) hardly changed: the downdraught is a robust feature of all variants. With wall functions at y+ of 30–300, k–ω SST behaves as a wall-function model rather than a low-Reynolds model, so the spread reflects the treatment of the stratified core rather than of the boundary layer at the glazing [25,26].

Radiator representation. Doubling the depth of the source changed the occupied-zone air temperature by 0.07 K and the peak near-façade speed by 1%, so the layer thickness of the first submission does not matter. The isothermal surface, the opposite limit, needed 81.9 °C (CA-R5) and 115.5 °C (DC-R6) to deliver the design output from a flat surface of the radiator outline, with a radiative fraction of 78–84%; real panel radiators, with a larger emitting area, emit 11–30% by radiation [41,42] and lie between the two limits. Delivering most of the heat by radiation lowered the occupied-zone air temperature by 0.8 K (CA-R5) and 1.5 K (DC-R6), halved the head–ankle difference (to 0.90 and 1.06 K) and weakened the rising plume, so the peak near-façade speed fell from 0.41 and 0.56 to 0.31 and 0.45 m/s. The maximum draught rate at the first row did not change (25 and 28%), because the radiators cover only the lower part of the façade and the downdraught from

the glazing reaches the floor in both limits (Figure S1). The conclusion on the draught at the first row therefore does not depend on the radiator model, whereas the air temperature and the stratification do.

These spreads enter the uncertainty of Section 3.7 together with the mesh and code effects.

3.6. Validation

3.6.1. V1: Downdraught Velocity Against the Correlation of Heiselberg

We simulated the CA-R5 room without heat sources at an outdoor temperature of −10 °C so that the glazing (height H = 2.55 m) was ΔT = 7.6 K colder than the occupied-zone air on the 0.15 m and 0.10 m meshes with the model of the courtroom cases (Section 2.6). The correlation of Heiselberg [3], as reproduced in [47,48], gives the maximum air speed near the floor at distance x from the cold surface:

$$u_{\max} = \begin{cases} 0.055\sqrt{\Delta T\, H} & \text{for } x < 0.4 \text{ m} \\ \dfrac{0.095\sqrt{\Delta T\, H}}{x + 1.32} & \text{for } 0.4 \text{ m} \le x \le 2.0 \text{ m} \\ 0.028\sqrt{\Delta T\, H} & \text{for } x > 2.0 \text{ m} \end{cases} \quad (14)$$

with u_{max} in m/s, ΔT in K and H and x in m. It was derived in an empty room with a two-dimensional flow from a cold surface reaching the floor; a heat load raises the maximum speed [49], CFD studies reproduce the correlation from about 0.5 m from the surface [47] and a CFD model with radiation reproduced the original maximum velocity with a mean relative error of 6.4% [48]. In the courtrooms the glazing starts 1.05 m above the floor, above a warmer parapet, so the correlation is an upper bound for the speeds of the real rooms.

Figure 5 and Table S5 compare the simulated and correlated speeds. On the 0.15 m mesh, the speed at 0.10 m above the floor was 0.61 (0.5–4.0 m from the façade) to 0.69 (0.5–2.0 m) of the correlation and the maximum below 0.3 m 0.72 to 0.83 of it; the simulated maximum, about 0.17–0.18 m/s, occurred 0.6–0.65 m from the façade. On the 0.10 m mesh, where the voxelised glazing is 2.60 m high and 7.4 K colder than the air (correlated speed within 1% of the 0.15 m value), these ratios rose to 0.68–0.83 and 0.87–1.01, so the underestimate shrinks with refinement, as the near-façade speeds of Section 3.2 do. The working mesh therefore underestimates the downdraught velocity by about 20–40%, and we read the simulated near-façade velocities and the draught rate at the first row of seats as lower estimates.

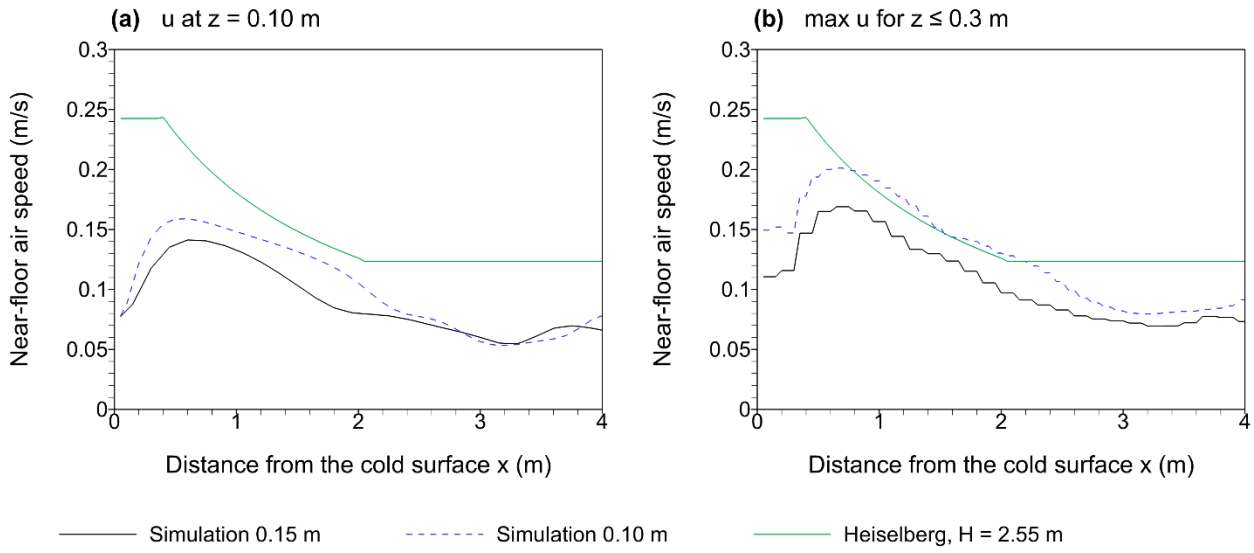


Figure 5. V1: air speed in the downdraught of the cold surface against the distance x from it, for CA-R5 without heat sources (model M1, mesh 0.15 m black solid line and 0.10 m blue dashed line), and correlation of Equation (13) for H = 2.55 m (green): (**a**) speed at 0.10 m above the floor; (**b**) maximum speed below 0.3 m above the floor.

3.6.2. V2: Measured Air Temperatures

Table 9 compares the simulated and measured air temperatures at the logger for the unoccupied periods (Section 2.6). The radiator output that reproduced the measured temperature on 8 February was 713 W in CA-R5 and 1026 W in DC-R6, about 55% of the transmission loss of Equation (6) for that night (1277 and 1881 W) in both rooms; with the full transmission loss, the simulated rooms were 1.4 and 2.1 K warmer than measured. A separate run at the calibrated output gave 22.42 °C against the measured 22.6 °C in CA-R5 and 20.55 °C against 20.7 °C in DC-R6, so the residual of the calibration is −0.18 and −0.15 K. The two other periods of CA-R5 are predictions with this output.

Table 9. Measured and simulated air temperature at the logger (1.1–1.5 m) in unoccupied quasi-steady periods (M1). Calibration rows show the check run at the calibrated output; prediction rows keep that output constant (main rule) and, in brackets, scale it with the outdoor temperature. Bias = mean ($T_{sim} - T_{meas}$); MAE = mean $|T_{sim} - T_{meas}|$; RMSE = root mean square of $T_{sim} - T_{meas}$.

Room	Period	T_e [°C]	T_{meas} [°C]	Q_{rad} [W]	T_{sim} [°C]	$T_{sim} - T_{meas}$ [K]	Role
CA-R5	8–9 February 2025	−3.7	22.6	713	22.42	−0.18	calibration
CA-R5	23 February 2025	−9.9	22.1	713 (892)	20.87 (21.71)	−1.23 (−0.39)	prediction
CA-R5	15–16 Mar 2025	3.9	24.9	713 (494)	23.17 (22.54)	−1.73 (−2.37)	prediction
DC-R6	8 February 2025	−3.7	20.7	1026	20.55	−0.15	calibration

For the two predictions with constant output, the bias was −1.48 K, the MAE 1.48 K and the RMSE 1.50 K (with weather-compensated output: −1.38, 1.38 and 1.69 K; Figure 6), three times the logger accuracy. The model underestimated the measured air temperature in both periods, by 1.2 K on 23 February and by 1.7 K on 15–16 March, when the real room was 2.3 K warmer than on the calibration night. Following the rule fixed before the runs, the neighbouring rooms of the 23 February prediction were set to the simulated room temperature because it differed from the calibration value by more than 0.3 K; with the neighbours kept at 22.6 °C, the error would have been −0.24 K (+0.23 K with compensated output). The prediction therefore depends mainly on two boundary conditions that were not measured, the heat actually supplied by the radiators and the temperature of the

adjacent rooms, rather than on the flow model. On 15–16 March, with the neighbours at 22.6 °C, the simulated room would have needed about 0.7 kW more than the calibrated output to reach the measured 24.9 °C (calibration slope 2.5 K/kW), which indicates a larger heat input than on 8 February (radiators that were not turned down in milder weather, or gains such as solar radiation, which the model omits).

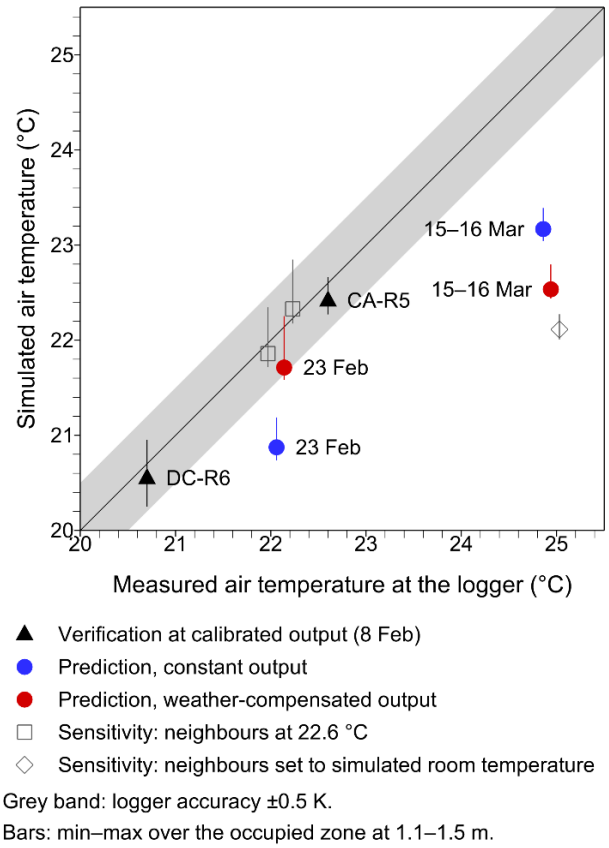


Figure 6. V2: simulated against measured air temperature at the logger (model M1, 0.15 m mesh): verification runs at the calibrated output (8 February, triangles), predictions with constant (blue) and weather-compensated output (red) and sensitivity runs with the neighbouring rooms at 22.6 °C and at the simulated room temperature (open symbols). Grey band: logger accuracy ±0.5 K; bars: minimum–maximum over the occupied zone at 1.1–1.5 m.

The low calibrated output does not by itself identify its cause. Infiltration during the unoccupied nights, which the model omits, neighbouring rooms colder than the logger room and transmittances higher than the assumed values would all require a smaller heat input to the model; we did not measure any of them. V2 therefore tests the predictive skill of the model under other outdoor conditions after the effective heat input has been calibrated, not its absolute heat balance. The head–ankle difference, the speeds and the draught rate are not validated by V2 and rest on V1 and on the analyses of Sections 3.2–3.5, which is why we call them indicative (Section 3.9).

3.7. Comfort Indicators

Existing state. The occupied-zone air temperature was 23.2–23.8 °C, 2.2–2.8 K above the 21 °C set-point, and the mean radiant temperature 19.8–20.3 °C, so the operative temperature (21.7–21.9 °C) stayed close to the set-point, with a mean PMV of −0.02 to 0.03 and a PPD of 5.1–5.2% (Table 10). The air above the occupied zone was a further 0.3–0.8 K

warmer. The high air temperature agrees with the 23.3–23.4 °C measured during the occupied hours of winter 2025 at much milder outdoor temperatures; the part-load runs (Section 3.8.1) and the calibration of V2 (Section 3.6) show that it results from the heat supply, not from the model, so the heating control rather than the envelope has to remove this overheating [50].

Table 10. Comfort indicators of M1: occupied-zone means (T_{op} = ($T_{air,occ}$ + T_{mrt})/2), mean percentage of dissatisfied (PPD), maximum velocity below 0.5 m within 0.6 m of the windowed walls ($u_{max,f}$), maximum ankle-level velocity in the first row of seats, 0.6–1.5 m from the façade ($u_{ankle,1}$) and maximum ankle-level draught rate there ($DR_{max,1}$). Values on the 0.15 m mesh. Uncertainty of the occupied-zone values (Section 2.6, Table S6): ±0.5 K (CA-R5) and ±1.0 K (DC-R6) for $T_{air,occ}$, ±0.8 K and ±1.2 K for $\Delta T_{1.1–0.1}$, ±2.5 and ±1.1 percentage points for DR.

Room	Sc.	Q_{rad} [W]	$T_{air,occ}$ [°C]	T_{mrt} [°C]	T_{op} [°C]	$\Delta T_{1.1–0.1}$ [K]	PMV	PPD [%]	DR [%]	DR_{P95} [%]	$u_{max,f}$ [m/s]	$u_{ankle,1}$ [m/s]	$DR_{max,1}$ [%]
CA-R5	S0	1117	23.2	20.3	21.7	1.3	−0.02	5.1	5.6	13.5	0.41	0.36	24.7
CA-R5	S1	804	23.0	20.5	21.8	1.2	−0.02	5.1	5.7	12.8	0.41	0.34	23.7
CA-R5	S2	316	22.8	20.6	21.7	1.0	−0.07	5.2	7.9	16.2	0.33	0.34	23.7
TR-R8	S0	1916	23.6	20.1	21.9	1.8	0.03	5.2	3.2	12.3	0.41	0.35	23.9
TR-R8	S1	1561	23.5	20.3	21.9	1.7	0.03	5.2	3.7	13.1	0.43	0.35	23.6
TR-R8	S2	809	23.1	20.5	21.8	1.2	−0.01	5.1	5.9	15.0	0.36	0.29	21.2
DC-R6	S0	2070	23.8	19.8	21.8	2.1	0.02	5.2	3.0	10.5	0.56	0.41	28.1
DC-R6	S1	1450	23.6	20.1	21.8	1.9	0.03	5.2	3.2	11.2	0.56	0.41	28.6
DC-R6	S2	0	23.0	20.9	22.0	1.1	0.04	5.1	3.6	11.3	0.26	0.26	17.8

Stratification. Between ankle (0.1 m) and head (1.1 m) height the air temperature rose by 1.3, 1.8 and 2.1 K in the existing state of CA-R5, TR-R8 and DC-R6 (Figure 7). These values come from the 0.15 m mesh, which overestimates the stratification: on the 0.075 m mesh, the difference was 0.7 K (CA-R5) and 1.2 K (DC-R6) in OpenFOAM and 0.6 and 1.1 K in Fluent. On the working mesh the existing state is below the 2 K limit of category A of ISO 7730 [45] in CA-R5 and TR-R8 and at the limit in DC-R6, and the finer mesh gives lower values; the uncertainty of ±0.8–1.2 K is, however, as large as the margin to the limit, so category A is not certain. With the reference model all cases are below the 3 K limit of category B, but with k–ω SST or with buoyancy production in the k–ε equations the existing DC-R6 reached 3.1–3.2 K (Section 3.5).

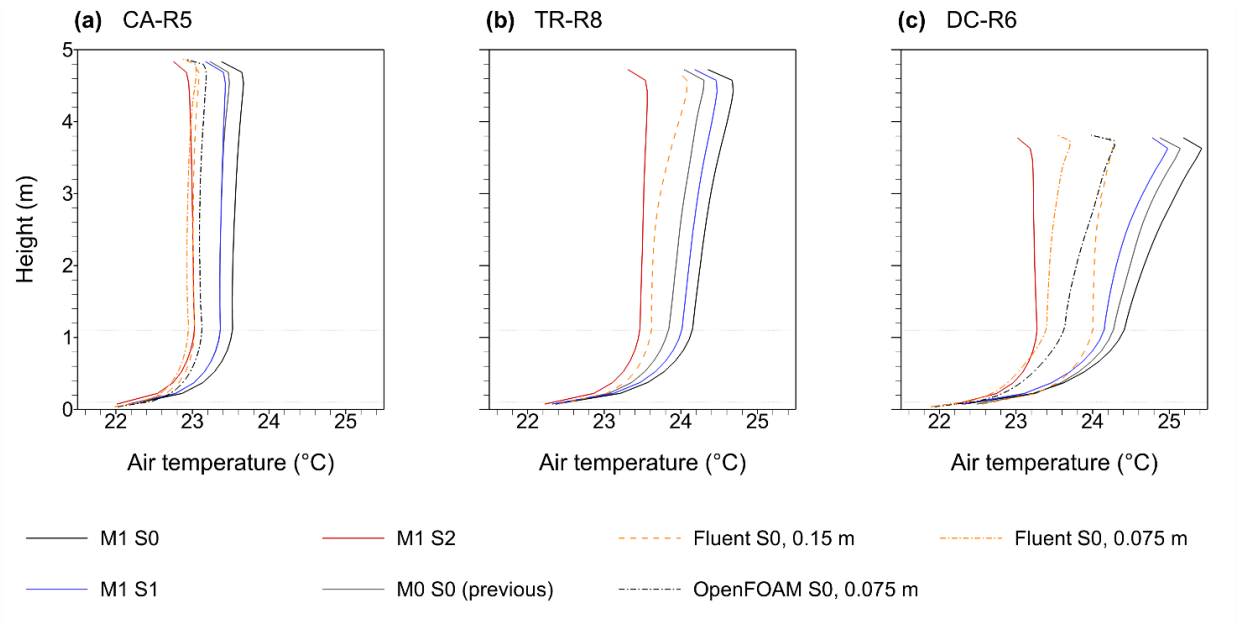


Figure 7. Vertical profiles of the air temperature, averaged horizontally over the plan area of the occupied zone, in (**a**) CA-R5, (**b**) TR-R8 and (**c**) DC-R6: model M1 on the 0.15 m mesh, S0 (black), S1 (blue) and S2 (red); for S0 also the previous model M0 (thin grey), Fluent on the 0.15 m mesh (orange dashed) and the 0.075 m mesh (dash-dot: OpenFOAM black, Fluent orange; CA-R5 and DC-R6 only).

Near-façade flow and local draught. The radiator plumes rose in front of the windows, but the radiators did not prevent the downdraught: cold air from the glazing and from the uninsulated wall below the sills reached the floor and spread into the first row of seats (Figures 3 and 8). The peak speed below 0.5 m within 0.6 m of the façade was 0.41 m/s in the insulated building and 0.56 m/s in DC-R6, and the maximum draught rate at the ankles of the first row was 24–29% in S0 and S1, above the 20% limit of category B; in S2 it was 21–24% in CA-R5 and TR-R8 and 18% in DC-R6. These maxima are local: less than 1.3% of the occupied zone exceeded DR = 20%, and the mean DR was 3.0–5.6% in the existing state and at most 7.9% after retrofit, within category A. The near-façade values are the least certain indicators. With Tu = 40% instead of the local value, the first-row maximum would be 29–52%, and V1 shows that the 0.15 m mesh underestimates the near-floor downdraught velocity by about 20–40% (ratio 0.61–0.83 to the correlation, 0.68–1.01 on the 0.10 m mesh); the peak near-façade speed increased by 0.07–0.11 m/s on the 0.075 m mesh. The reported draught at the first row is therefore more likely to be underestimated than overestimated.

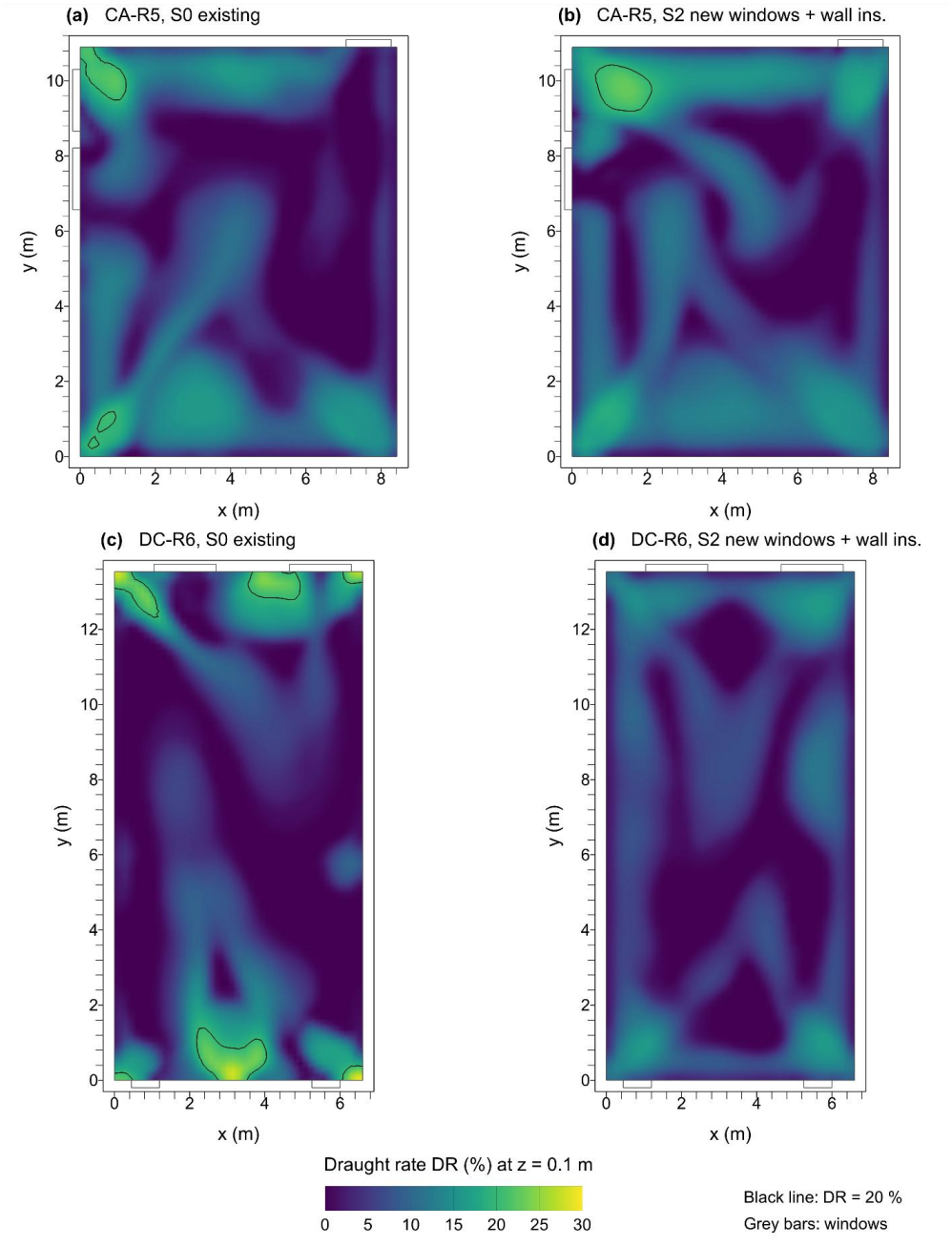


Figure 8. Draught rate DR at 0.1 m above the floor (ISO 7730, local turbulence intensity; model M1, 0.15 m mesh): (**a**) CA-R5, S0; (**b**) CA-R5, S2; (**c**) DC-R6, S0; (**d**) DC-R6, S2. Black line: DR = 20%; grey bars: windows.

Effect of the retrofit. Window replacement raised the mean inner glazing temperature from 13.0–13.1 to 16.6–16.7 °C in CA-R5 and TR-R8 and from 8.9 to 17.9 °C in DC-R6 (Figure S3). With the radiator output reduced accordingly (Table 2), the operative temperature stayed at 21.7–22.0 °C, while from S0 to S2 the air temperature fell by 0.4, 0.5 and 0.8 K and the mean radiant temperature rose by 0.3, 0.4 and 1.1 K. The head–ankle difference fell to 1.2–1.9 K in S1 and 1.0–1.2 K in S2. In DC-R6 window replacement alone left the first-row draught unchanged (maximum DR 28.1 and 28.6%), because the uninsulated wall below the sills still cooled the air; wall insulation reduced the peak near-façade speed from 0.56 to 0.26 m/s and the first-row maximum DR to 17.8%. In the insulated building the windows were the main cold surface and their replacement changed the first-row maximum DR only by about 1 percentage point. The mean DR rose slightly after retrofit (CA-R5 5.6 to 7.9%, TR-R8 3.2 to 5.9%), probably because the cooler air and the weaker

radiator plumes leave more of the room to the slower, cooler recirculation. All nine cases met category A of ISO 7730 for the PMV and the mean draught rate.

3.8. Heating Demand and Ventilation

3.8.1. Design Condition, Ventilation and Part Load

Transmission loss. At the design condition, window replacement cut the transmission loss by 16% in CA-R5, 13% in TR-R8 and 21% in DC-R6 and its combination with wall insulation by 40%, 39% and 75% (Table 2; independent of the CFD). The radiator output dropped more (by 19–30% in S1 and 58–100% in S2) because the occupant gains stay constant. In DC-R6 S2 the remaining loss (733 W) fell below the sensible gains of 12 occupants (900 W), so a room without ventilation needed no radiator output during hearings.

Ventilation. At the EN 16798-1 rate (146.5–148.2 L/s, Equation (8)), the design loss of the ventilation flow is 6.9–7.0 kW (Equation (9)), 2.3–3.5 times the transmission loss of the existing rooms and 4–9 times that after the full retrofit; 75% sensible recovery cuts it to about 1.7 kW. Table 11 compares the ventilation cases with the same rooms without ventilation, and Figure 9 shows the draught rate at ankle height.

Table 11. Ventilation cases against the same case without ventilation (M1): radiator output, heat delivered to the supply air outside the room, $T_{air,occ}$, T_{op}, $\Delta T_{1.1–0.1}$, mean and 95th-percentile DR, share of the occupied zone with DR > 20% and first-row maximum DR ($DR_{max,1}$). V-a, V-b and V-c: supply air at 21, 12 and 18 °C (Section 2.4.4).

Room, Scenario	Case	Q_{rad} [W]	Heat to Supply Air [W]	$T_{air,occ}$ [°C]	T_{op} [°C]	$\Delta T_{1.1–0.1}$ [K]	DR [%]	DR_{P95} [%]	Share DR > 20% [%]	$DR_{max,1}$ [%]
CA-R5 S0	none	1117	0	23.2	21.7	1.3	5.6	13.5	0.2	24.7
CA-R5 S0	V-a	1117	259	22.4	21.2	0.9	6.6	15.1	0.5	24.6
CA-R5 S0	V-b	2726	1880	21.5	20.7	0.6	12.3	37.2	19.2	43.5
CA-R5 S0	V-c	1670	757	22.1	21.1	0.7	8.2	18.4	2.1	21.6
DC-R6 S2	none	0	0	23.0	22.0	1.1	3.6	11.3	0.0	17.8
DC-R6 S2	V-a	0	194	22.0	21.3	0.6	9.0	19.3	3.1	24.8
DC-R6 S2	V-b	1423	1765	21.1	20.8	0.4	13.6	33.5	19.5	31.4
DC-R6 S2	V-c	379	693	21.7	21.1	0.4	12.4	25.8	15.5	32.2

With supply air at 21 °C (V-a), the occupied zone was 22.0–22.4 °C, the stratification fell to 0.6–0.9 K and the mean DR rose to 6.6–9.0% with at most 3.1% of the occupied zone above DR = 20%. With supply air at 12 °C after heat recovery and no reheating (V-b), the cool jet fell into the occupied zone: the mean DR rose to 12.3–13.6%, 19% of the occupied zone exceeded DR = 20% and the operative temperature dropped to 20.7–20.8 °C, even though the radiators delivered 2.7 kW (CA-R5) and 1.4 kW (DC-R6). Reheating the supply air to 18 °C (V-c) was enough in CA-R5, where the radiators still deliver 1.7 kW along the façade (2.1% of the zone above DR = 20%), but not in the retrofitted DC-R6, where they deliver only 0.4 kW (15.5% of the zone above 20%).

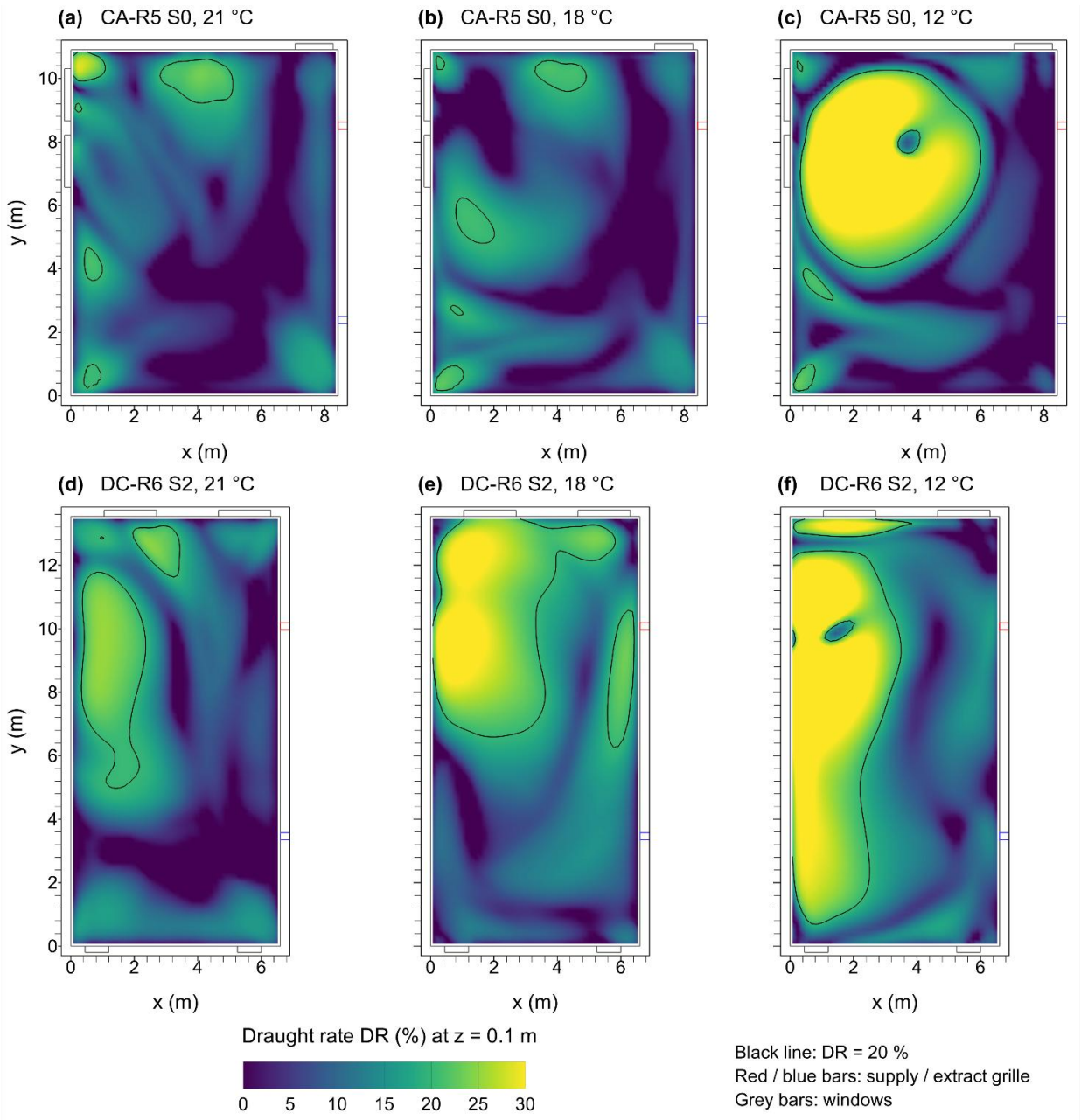


Figure 9. Draught rate DR at 0.1 m above the floor in the ventilation cases (model M1, 0.15 m mesh) with supply air at 21, 18 and 12 °C (V-a, V-c, V-b): (**a**–**c**) CA-R5, S0; (**d**–**f**) DC-R6, S2. Black line: DR = 20%; red and blue bars: supply and extract grille; grey bars: windows.

Reassessment of the DC-R6 conclusion. The first submission concluded that the fully retrofitted DC-R6 needed no radiator output during hearings. That holds only for the room without ventilation. With the supply air tempered to 21 °C (V-a), the radiators stay off, but the demand moves to the air-handling unit (about 7 kW without recovery and 1.7 kW with 75% recovery at the design condition). With the supply air at 12 °C after recovery (V-b), the room needs 1.42 kW of radiator output (1.46 kW from the energy balance at 150 L/s), 69% of the existing-state output, and the cool supply causes local draught. After a deep envelope retrofit, the supply air should therefore be reheated close to room temperature or delivered through high-induction diffusers.

Part load. At an outdoor temperature of 0 °C, radiators that keep the design output (no control) raised the occupied-zone air to 24.8 °C in CA-R5 and 26.1 °C in DC-R6 (oper-

ative temperature 23.4 and 24.1 °C, PMV 0.33 and 0.52). With the output scaled in proportion to the indoor–outdoor temperature difference (weather compensation), the air was 23.6 and 24.2 °C and the operative temperature 22.4 and 22.5 °C; at the mean outdoor temperature of the heating season (4.5 °C), these values were 23.7–24.2 °C and 22.6–22.7 °C. The retrofitted DC-R6 without radiator output reached 23.6 °C at 0 °C. The occupants, the neighbouring rooms at 21 °C and the steady state keep the rooms warm at part load even with weather-compensated output, which is consistent with the measured overheating and shows that the rooms need a control that responds to the room temperature, not only to the outdoor temperature.

Relative humidity and air quality. At the design condition of −18 °C, outdoor air holds about 0.65 g/kg of water vapour. Twelve seated persons release about 0.6 kg/h of moisture, which adds only about 1 g/kg at 150 L/s, so the indoor relative humidity (RH) would be about 10% at 22 °C, well below the winter mean measured in CA-R5 (24%). The design condition is the extreme case: over eight seasons the modelled RH during hearings is higher (Section 3.8.2). Such dry air affects the eyes, the airways and perceived air quality [51,52]: low periocular RH thins the tear film [53], 10% RH shortened the tear break-up time relative to 45% RH [54] and humidification is a recognised measure against dryness symptoms [55]. Speakers use their voice for hours, so dryness of the mucous membranes is a plausible concern.

A lower ventilation rate raises the RH but worsens air quality and raises the infection risk [19]. Demand-controlled ventilation cuts the outdoor flow in a lightly occupied room. Enthalpy recovery returns part of the room moisture to the supply air, which a sensible-only exchanger does not [56,57], although frost limits recovery in the cold [58]. Active humidification adds a latent load and a condensation risk: at 21 °C, the coldest part of the existing DC-R6 glazing (5.3 °C in the revised model, mean 8.9 °C) reaches the dew point at about 36% RH (46% for the mean), whereas the replaced glazing (14.4 °C minimum, 17.9 °C mean) tolerates about 66% RH.

3.8.2. Seasonal Heating Demand and Indoor Humidity

The design condition overstates the annual demand, so we added an hourly analytical model (no CFD) driven by the hourly METAR record of Iași airport (LRIA, about 4 km away) for eight seasons, 2018/19–2025/26. Heating ran from 15 October to 15 April on days with a mean outdoor temperature below 12 °C, at a constant 21 °C. Ventilation followed EN 16798-1 category II [44] during hearings only (08:00–16:00, working days), with infiltration of 0.1 ACH, sensible gains of 75 W per person, no solar gains and the transmission coefficients of Table 2. V0 had no recovery, V1 a sensible efficiency of 0.75 and V2 in addition a moisture-recovery efficiency of 0.6; both efficiencies are assumptions, below the sensible and latent effectiveness of 0.8 and 0.7 reported for membrane total-heat exchangers [59], as is the moisture release of 50 g/h per person.

Table 12 and Figure 10 give the demand. Without recovery (S0/V0) it was 69, 86 and 87 kWh/m² per season in CA-R5, TR-R8 and DC-R6; mechanical ventilation accounted for 25–31% of it and for 33–48% in S2/V0. Full retrofit with sensible recovery (S2/V1) cut it by 51, 49 and 74%.

Table 12. Seasonal heating demand [kWh/m² per season]: mean of eight seasons and, in brackets, the range. S0, existing state; S2, window replacement with wall insulation; V0, no heat recovery; V1, sensible recovery (0.75). V2 has the same sensible demand as V1.

Room	S0/V0	S2/V0	S2/V1
CA-R5	69.0 (59.8–75.5)	53.6 (46.6–58.9)	33.5 (28.7–36.3)
TR-R8	85.5 (74.1–93.3)	63.7 (55.3–69.9)	43.3 (37.1–46.9)
DC-R6	87.1 (75.4–95.0)	42.6 (37.2–47.2)	22.4 (19.1–24.3)

During hearings the modelled indoor RH at 21 °C had a median of 30% without moisture recovery (V0, V1; 10th–90th percentile 20–43%) and was below 30% in 47% of the hours; with V2 the median was 37–38% and 17–20% of the hours were below 30%. With 40–70 g/h per person and a moisture efficiency of 0.5–0.7, the share of V2 h below 30% ranged from 1 to 37%, so the benefit of enthalpy recovery depends on assumptions we did not verify. The V0 median agrees with the winter-2025 measurement in CA-R5 (22.8% measured, 21.9% modelled at the measured air temperature), but this agreement is partly coincidental: no mechanical ventilation is known in the room, so the 148 L/s represents an effective air exchange of that order, not a measured rate. The model is quasi-steady, without moisture sorption, and omits the energy for humidification.

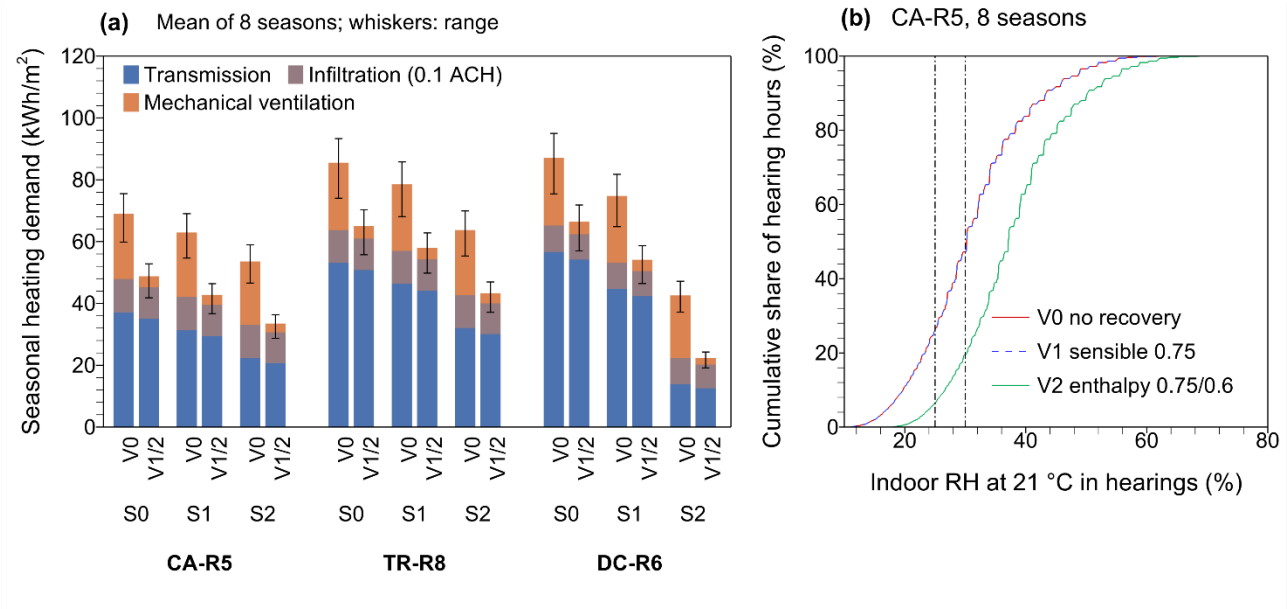


Figure 10. Seasonal analysis (eight heating seasons, hourly weather data of Iași airport): (**a**) heating demand by loss path for the three rooms, scenarios S0–S2 and recovery options V0 and V1/V2, mean with range of the seasons; (**b**) cumulative distribution of the indoor relative humidity at 21 °C during hearings in CA-R5, with the 25% and 30% limits (dash-dotted).

3.9. Limitations

The following idealisations bound the accuracy of the absolute values; we give the indicators with the uncertainty of Sections 3.2–3.7.

1. **Envelope.** The U-values (Table 2, U_{int}), window and radiator dimensions are typical values or assumptions; no envelope survey, heat-flow measurement or radiator data were available.
2. **Interior boundary.** Neighbouring rooms are at a fixed 21 °C; at 23 °C the occupied-zone air would be 1.9 K warmer (CL-N23), so the absolute air temperature depends on this assumption.

3. **Radiation.** The model is grey and diffuse, with transparent air, agglomerated view factors and one glazing emissivity; solar, lighting and equipment gains are not modelled.
4. **Heat sources.** Radiators are volumetric sources or, in the sensitivity runs, isothermal surfaces that bound the real radiative share; the occupants are a uniform convective source of 900 W, without bodies, furniture or their own plume.
5. **Turbulence and walls.** Steady RANS with wall functions cannot resolve natural-convection boundary layers (Section 2.3) and the averaged fields represent the weakly unsteady flow, so near-façade velocity and DR are indicative.
6. **Validation.** V2 covers one air temperature per room (the logger position was not recorded; we used the room-centre column at 1.1–1.5 m), after calibrating the heat input, with two independent predictions in CA-R5; V1 covers the velocity scale of a simple geometry; the velocity field, vertical profile and surface temperatures are not validated.
7. **Ventilation.** One supply layout with three supply temperatures, dry air, no infiltration (which would add to the load); the relative humidity comes from an analytical balance.
8. **Operation.** We simulated the steady design condition, two steady part-load conditions and quasi-steady unoccupied periods; intermittent operation, thermal mass and the dynamics of heating control are not represented.
9. **Comfort evaluation.** The PMV assumes 1.0 clo, 1.2 met and 35% RH, although the measured RH was lower (24–29%); the DR uses the RANS turbulent kinetic energy as a proxy for the turbulence intensity, which steady RANS with wall functions represents poorly near the façade (with Tu = 40% instead of the local value the first-row maximum rose from 18–29% to 29–52% in M1), so the category of local draught is uncertain; the thermography was used qualitatively.

These limits do not change the ranking of the scenarios, which was the same in both codes, all turbulence models and both radiator representations (Sections 3.3–3.5).

4. Conclusions

We combined infrared thermography, steady CFD with surface radiation and a coupled envelope, and ventilation and part-load cases to assess window replacement and external wall insulation in three courtrooms in Iași at −18 °C.

1. **Envelope.** The glazing was the weakest element of the recent building. Window replacement cut the design transmission loss by 13–21% and raised the mean glazing temperature to 16.6–17.9 °C; with wall insulation the loss fell by 39–75%.
2. **Comfort and draught.** In all nine cases the mean PMV was −0.07 to 0.04 and the mean draught rate 3.0–7.9%. The head–ankle difference (1.0–2.1 K on the working mesh, 0.7–1.2 K on the finer mesh) met category B with the reference model but reached 3.1–3.2 K in the existing DC-R6 with two of the turbulence models. The radiators did not prevent local draught: at the ankles of the first row the maximum DR was 24–29% before and 18–24% after wall insulation, in all turbulence models and both radiator representations, and probably higher in reality.
3. **Air temperature and heat supply.** Radiation changed the occupied-zone air temperature by only 0.1–0.2 K; the air stayed 2.2–2.8 K above 21 °C. The measurements were reproduced with about 55% of the computed transmission loss as heat input, and uncontrolled radiators overheated the rooms at part load (24.8–26.1 °C at 0 °C), so heating control comes before the envelope measures.
4. **Reliability.** OpenFOAM and Fluent agreed on the heat balance and, on the finer meshes, on the air temperature within 0.2 K. The occupied-zone air temperature is

uncertain by ±0.5–1.0 K, plus 1.9 K if the neighbouring rooms are at 23 °C; the working mesh underestimates the downdraught velocity by 20–40%; after calibration of the heat input, the model predicted the measured air temperature in two further periods with an MAE of 1.5 K, limited mainly by the unmeasured heat supply and temperature of the adjacent rooms.

5. **Ventilation.** At the EN 16798-1 rate, the ventilation loss (6.9–7.0 kW) is 4–9 times the transmission loss after full retrofit; 75% sensible recovery cuts it to 1.7 kW. Supply air at 12 °C after recovery put 19% of the occupied zone above DR = 20% and still required 1.4 kW of radiator output in the retrofitted DC-R6; reheating to 18 °C was enough only where the radiators still heat the façade. Over eight seasons, full retrofit with sensible recovery lowered the demand by 49–74%, and enthalpy recovery reduced the hearing hours below 30% RH from 47% to 17–20%.

Recommendation. Envelope retrofit alone is not enough, because ventilation becomes the largest loss and the main cause of dry air. Courtrooms need room-temperature control of the radiators and demand-controlled ventilation with enthalpy recovery, designed together with the envelope; after a deep retrofit the supply air should be reheated close to room temperature or delivered through high-induction diffusers, and wall insulation is needed where first-row draught matters.

Validity. The results hold for the design condition and the assumed envelope, and the validation is partial (Section 3.9). Mean temperatures, heat flows and the ranking of the scenarios are robust; the stratification, near-façade velocities, draught rates and seasonal humidity are indicative. Future work should measure velocity, turbulence and temperature profiles in an occupied courtroom.

Supplementary Materials: The following supporting information can be downloaded at https://www.mdpi.com/article/10.3390/thermo6040091/s1: Supplementary Material S1: grid convergence of the original and revised models (Tables S1a and S1b), convergence of the OpenFOAM and Ansys Fluent cases (Tables S2a and S2b), mesh quality and wall distance y+ (Tables S3a and S3b), heat balance (Table S4), downdraught validation V1 (Table S5), uncertainty components of the occupied-zone indicators (Table S6), radiator representation (Figure S1), comparison of OpenFOAM and Fluent in the window section (Figure S2) and interior surface temperature of the main façade (Figure S3).

Author Contributions: Conceptualization, methodology, software, validation, formal analysis, investigation, resources, data curation, writing—original draft preparation, writing—review and editing, visualization and supervision: C.C.V., F.-E.Ț., V.-S.H., C.-N.C., C.R., C.O., D.U., A.A.Ș. and C.G.P. All authors contributed equally to this work. All authors have read and agreed to the published version of the manuscript.

Funding: This research received no external funding.

Data Availability Statement: The data presented in this study are available upon request from the corresponding author.

Conflicts of Interest: The authors declare no conflicts of interest.

Abbreviations

The following abbreviations are used in this manuscript:

CFD	Computational fluid dynamics
PMV	Predicted mean vote
PPD	Predicted percentage of dissatisfied
DR	Draught rate
RH	Relative humidity

ACH	Air changes per hour
CA-R5, DC-R6, TR-R8	Room 5 of the Court of Appeal, Room 6 of the District Court, Room 8 of the Tribunal
DCV	Demand-controlled ventilation
ERV	Energy recovery ventilator
GCI	Grid convergence index
IAQ	Indoor air quality
IRT	Infrared thermography
M0, M1	Reference model (prescribed surface temperatures), revised model (radiation, coupled envelope)
MAE	Mean absolute error
RANS	Reynolds-averaged Navier–Stokes
RMSE	Root-mean-square error
S0, S1, S2	Existing state, window replacement, window replacement with wall insulation
S2S	Surface-to-surface radiation model
T_{mrt}	Mean radiant temperature
T_{op}	Operative temperature

References

1. European Parliament; Council of the European Union. Directive (EU) 2024/1275 of 24 April 2024 on the Energy Performance of Buildings (Recast). *Off. J. Eur. Union* **2024**, *L 2024/1275*, 8 May 2024. Available online: http://data.europa.eu/eli/dir/2024/1275/oj (accessed on 22 November 2026).
2. European Parliament; Council of the European Union. Directive (EU) 2023/1791 of 13 September 2023 on Energy Efficiency and Amending Regulation (EU) 2023/955 (Recast). *Off. J. Eur. Union* **2023**, *L 231*, 1–111.
3. Heiselberg, P. Draught risk from cold vertical surfaces. *Build. Environ.* **1994**, *29*, 297–301. https://doi.org/10.1016/0360-1323(94)90026-4.
4. Myhren, J.A.; Holmberg, S. Flow patterns and thermal comfort in a room with panel, floor and wall heating. *Energy Build.* **2008**, *40*, 524–536. https://doi.org/10.1016/j.enbuild.2007.04.011.
5. Maivel, M.; Ferrantelli, A.; Kurnitski, J. Experimental determination of radiator, underfloor and air heating emission losses due to stratification and operative temperature variations. *Energy Build.* **2018**, *166*, 220–228. https://doi.org/10.1016/j.enbuild.2018.01.061.
6. Võsa, K.-V.; Ferrantelli, A.; Kurnitski, J. Assessment of downward draught in high-glazing facades in cold climates—Experimental and CFD study into draught control with a 21-type radiator. *E3S Web Conf.* **2021**, *246*, 02002. https://doi.org/10.1051/e3sconf/202124602002.
7. Wu, Q.; Xu, W.; Zhu, Y.; Liu, J. Optimization for the temperature range of radiator for preventing draught risk of cold window. *Energy Build.* **2024**, *323*, 114815. https://doi.org/10.1016/j.enbuild.2024.114815.
8. Wu, Q.; Wang, Z.; Dong, J.; Liu, J. A method for judging the overheating of the radiator in the compensation of window down-draught based on thermal image velocimetry. *Build. Environ.* **2021**, *197*, 107858. https://doi.org/10.1016/j.buildenv.2021.107858.
9. Nielsen, P.V. Fifty years of CFD for room air distribution. *Build. Environ.* **2015**, *91*, 78–90. https://doi.org/10.1016/j.buildenv.2015.02.035.
10. Chen, Q. Ventilation performance prediction for buildings: A method overview and recent applications. *Build. Environ.* **2009**, *44*, 848–858. https://doi.org/10.1016/j.buildenv.2008.05.025.
11. Weller, H.G.; Tabor, G.; Jasak, H.; Fureby, C. A tensorial approach to computational continuum mechanics using object-oriented techniques. *Comput. Phys.* **1998**, *12*, 620–631. https://doi.org/10.1063/1.168744.
12. Limane, A.; Fellouah, H.; Galanis, N. Three-dimensional OpenFOAM simulation to evaluate the thermal comfort of occupants, indoor air quality and heat losses inside an indoor swimming pool. *Energy Build.* **2018**, *167*, 49–68. https://doi.org/10.1016/j.enbuild.2018.02.037.
13. Ciocan, V.; Țurcanu, E.F.; Verdeș, M.; Luciu, R.S.; Bălan, M.C.; Hudișteanu, S.V.; Burlacu, A. Thermal comfort assessment for different heating system using CFD-modelling inside of an orthodox church. *IOP Conf. Ser. Mater. Sci. Eng.* **2019**, *586*, 012042. https://doi.org/10.1088/1757-899x/586/1/012042.
14. Aste, N.; Torre, S.D.; Adhikari, R.S.; Buzzetti, M.; Del Pero, C.; Leonforte, F.; Cardenas, H.E.H. CFD Comfort Analysis of a Sustainable Solution for Church Heating. *Energy Procedia* **2017**, *105*, 2797–2802. https://doi.org/10.1016/j.egypro.2017.03.603.

15. Vallati, A.; Di Matteo, M.; Fiorini, C.V. Retrofit proposals for energy efficiency and thermal comfort in historic public buildings: The case of the Engineering Faculty's seat of Sapienza University. *Energies* **2023**, *16*, 151. https://doi.org/10.3390/en16010151.
16. Fatahian, E.; Awwal, S.; Mishra, R.; Fleming, L.; Fatahian, H. Healthy and energy-efficient building retrofits: A systematic review of CFD, digital twins, and occupant-centred intelligence. *Build. Environ.* **2026**, *304*, 115073. https://doi.org/10.1016/j.buildenv.2026.115073.
17. Wu, J.; Chen, Y.; Deng, Y. Impact of winter air supply strategies on thermal comfort in yamen buildings: A case study of the Jiangsu Provincial Judicial Commissioner's Office. *Atmosphere* **2025**, *17*, 38. https://doi.org/10.3390/atmos17010038.
18. Martin, S.B.; Coffey, C.C. An indoor environmental quality investigation of the Fayette County (Pennsylvania) Courthouse. *Indoor Built Environ.* **2007**, *16*, 456–464. https://doi.org/10.1177/1420326X07082791.
19. Vernez, D.; Schwarz, S.; Sauvain, J.-J.; Petignat, C.; Suarez, G. Probable aerosol transmission of SARS-CoV-2 in a poorly ventilated courtroom. *Indoor Air* **2021**, *31*, 1776–1785. https://doi.org/10.1111/ina.12866.
20. Malhotra, M.; Im, P.; New, J. A process for defining prototype building models: Courthouse case study for U.S. commercial energy. *Energies* **2019**, *12*, 4020. https://doi.org/10.3390/en12204020.
21. Nindartin, A.; Moon, H.-W.; Park, S.-J.; Lee, K.-T.; Im, J.-B.; Kim, J.-H. Influencing of the building energy policies upon the efficiency of energy consumption: The case of courthouse buildings in South Korea. *Energies* **2022**, *15*, 6679. https://doi.org/10.3390/en15186679.
22. Chen, Q. Comparison of different k-ε models for indoor air flow computations. *Numer. Heat Transf. B Fundam.* **1995**, *28*, 353–369. https://doi.org/10.1080/10407799508928838.
23. Zhai, Z.J.; Zhang, Z.; Zhang, W.; Chen, Q.Y. Evaluation of various turbulence models in predicting airflow and turbulence in enclosed environments by CFD: Part 1—Summary of prevalent turbulence models. *HVAC R Res.* **2007**, *13*, 853–870. https://doi.org/10.1080/10789669.2007.10391459.
24. Blocken, B. LES over RANS in building simulation for outdoor and indoor applications: A foregone conclusion? *Build. Simul.* **2018**, *11*, 821–870. https://doi.org/10.1007/s12273-018-0459-3.
25. Zhang, Z.; Zhang, W.; Zhai, Z.J.; Chen, Q.Y. Evaluation of Various Turbulence Models in Predicting Airflow and Turbulence in Enclosed Environments by CFD: Part 2—Comparison with Experimental Data from Literature. *HVAC R Res.* **2007**, *13*, 871–886. https://doi.org/10.1080/10789669.2007.10391460.
26. Hirano, Y.; Katoh, M.; Yumino, S.; Okaze, T. Validation of Turbulence Models used in CFD Analysis of Indoor Natural Convection with a Cold Window and a Thermal Manikin. *E3S Web Conf.* **2026**, *716*, 03015. https://doi.org/10.1051/e3sconf/202671603015.
27. Tamrakar, S.; Chen, L.; Sørensen, B.R. Variation of Mean Radiant Temperature in Rooms for Summer and Winter Conditions. *Energies* **2023**, *16*, 5609. https://doi.org/10.3390/en16155609.
28. Marigo, M.; Tognon, G.; De Carli, M.; Zarrella, A. Effects of radiant asymmetry on the thermal comfort conditions: Experiments in a test room. *Appl. Therm. Eng.* **2024**, *248*, 123248. https://doi.org/10.1016/j.applthermaleng.2024.123248.
29. Sørensen, D.N.; Nielsen, P.V. Quality control of computational fluid dynamics in indoor environments. *Indoor Air* **2003**, *13*, 2–17. https://doi.org/10.1111/j.1600-0668.2003.00170.x.
30. Roache, P.J. Quantification of uncertainty in computational fluid dynamics. *Annu. Rev. Fluid Mech.* **1997**, *29*, 123–160. https://doi.org/10.1146/annurev.fluid.29.1.123.
31. Oberkampf, W.L.; Trucano, T.G. Verification and validation in computational fluid dynamics. *Prog. Aerosp. Sci.* **2002**, *38*, 209–272. https://doi.org/10.1016/s0376-0421(02)00005-2.
32. Celik, I.B.; Ghia, U.; Roache, P.J.; Freitas, C.J.; Coleman, H.; Raad, P.E. Procedure for Estimation and Reporting of Uncertainty Due to Discretization in CFD Applications. *J. Fluids Eng.* **2008**, *130*, 078001. https://doi.org/10.1115/1.2960953.
33. Kylili, A.; Fokaides, P.A.; Christou, P.; Kalogirou, S.A. Infrared thermography (IRT) applications for building diagnostics: A review. *Appl. Energy* **2014**, *134*, 531–549. https://doi.org/10.1016/j.apenergy.2014.08.005.
34. Lucchi, E. Applications of the infrared thermography in the energy audit of buildings: A review. *Renew. Sustain. Energy Rev.* **2018**, *82*, 3077–3090. https://doi.org/10.1016/j.rser.2017.10.031.
35. Fox, M.; Coley, D.; Goodhew, S.; de Wilde, P. Thermography methodologies for detecting energy related building defects. *Renew. Sustain. Energy Rev.* **2014**, *40*, 296–310. https://doi.org/10.1016/j.rser.2014.07.188.
36. Launder, B.E.; Spalding, D.B. The numerical computation of turbulent flows. *Comput. Methods Appl. Mech. Eng.* **1974**, *3*, 269–289. https://doi.org/10.1016/0045-7825(74)90029-2.
37. *EN ISO 6946:2017*; Building Components and Building Elements—Thermal Resistance and Thermal Transmittance—Calculation Methods. International Organization for Standardization: Geneva, Switzerland, 2017.

38. MDLPA. Metodologie de Calcul al Performanței Energetice a Clădirilor, Indicativ Mc 001-2022 (Approved by Ordinul MDLPA nr. 16/2023). *Monitorul Oficial al României*, 17 January 2023; Partea I, nr. 46 and annex 46 bis.
39. Li, X.; Yan, Y.; Tu, J. Evaluation of models and methods to simulate thermal radiation in indoor spaces. *Build. Environ.* **2018**, *144*, 259–267. https://doi.org/10.1016/j.buildenv.2018.08.033.
40. Teodosiu, C.; Kuznik, F.; Teodosiu, R. CFD modeling of buoyancy driven cavities with internal heat source—Application to heated rooms. *Energy Build.* **2014**, *68*, 403–411. https://doi.org/10.1016/j.enbuild.2013.09.041.
41. Yoshino, H.; Ishikawa, Y.; Nagatomo, M.; Sasaki, K. Measurement on the amount of thermal radiation of hot water panel. *AIJ J. Technol. Des.* **1996**, *2*, 140–143. https://doi.org/10.3130/aijt.2.140.
42. Muniak, D.P. *Radiators in Hydronic Heating Installations*; Springer: Cham, Switzerland, 2017. https://doi.org/10.1007/978-3-319-55242-2.
43. Peng, Z.; Carrigan, S.; Kornadt, O. Numerical investigation of the heat transfer in realistic rooms with a two-panel radiator. *Build. Simul. Conf. Proc.* **2023**, *18*, 1546–1553. https://doi.org/10.26868/25222708.2023.1242.
44. *EN 16798-1:2019*; Energy Performance of Buildings—Ventilation for Buildings—Part 1: Indoor Environmental Input Parameters for Design and Assessment of Energy Performance of Buildings Addressing Indoor Air Quality, Thermal Environment, Lighting and Acoustics—Module M1-6. European Committee for Standardization: Brussels, Belgium, 2019.
45. *ISO 7730:2005*; Ergonomics of the Thermal Environment—Analytical Determination and Interpretation of Thermal Comfort Using Calculation of the PMV and PPD Indices and Local Thermal Comfort Criteria. International Organization for Standardization: Geneva, Switzerland, 2005.
46. Fanger, P.O.; Melikov, A.K.; Hanzawa, H.; Ring, J. Air turbulence and sensation of draught. *Energy Build.* **1988**, *12*, 21–39. https://doi.org/10.1016/0378-7788(88)90053-9.
47. Jurelionis, A.; Isevičius, E. CFD predictions of indoor air movement induced by cold window surfaces. *J. Civ. Eng. Manag.* **2008**, *14*, 29–38. https://doi.org/10.3846/1392-3730.2008.14.29-38.
48. Joe, G.; Kim, D.; Park, S.; Park, S.; Yeo, M.; Kim, K. Downdraft Assessment of Glass Curtain Wall Buildings with a Radiant Floor Heating System. *Appl. Sci.* **2017**, *7*, 1075. https://doi.org/10.3390/app7101075.
49. Manz, H.; Frank, T. Analysis of Thermal Comfort Near Cold Vertical Surfaces by Means of Computational Fluid Dynamics. *Indoor Built Environ.* **2004**, *13*, 233–242. https://doi.org/10.1177/1420326x04043733.
50. Hoyt, T.; Arens, E.; Zhang, H. Extending air temperature setpoints: Simulated energy savings and design considerations for new and retrofit buildings. *Build. Environ.* **2015**, *88*, 89–96. https://doi.org/10.1016/j.buildenv.2014.09.010.
51. Wolkoff, P. Indoor air humidity, air quality, and health—An overview. *Int. J. Hyg. Environ. Health* **2018**, *221*, 376–390. https://doi.org/10.1016/j.ijheh.2018.01.015.
52. Derby, M.M.; Hamehkasi, M.; Eckels, S.; Fenton, D.; Horwath, P.; Maghirang, R.; Rongere, F.-X. Update of the scientific evidence for specifying lower limit relative humidity levels for comfort, health, and indoor environmental quality in occupied spaces (RP-1630). *Sci. Technol. Built Environ.* **2017**, *23*, 30–45. https://doi.org/10.1080/23744731.2016.1206430.
53. Wolkoff, P.; Nojgaard, J.K.; Franck, C.; Skov, P. The modern office environment desiccates the eyes? *Indoor Air* **2006**, *16*, 258–265. https://doi.org/10.1111/j.1600-0668.2006.00429.x.
54. Ito, K.; Takada, S. Effects of indoor low humidity on eye discomfort and associated physiological responses in soft contact lens and non-lens wearers. *Indoor Built Environ.* **2022**, *32*, 590–602. https://doi.org/10.1177/1420326x221126352.
55. Byber, K.; Radtke, T.; Norbäck, D.; Hitzke, C.; Imo, D.; Schwenkglenks, M.; Puhan, M.A.; Dressel, H.; Mutsch, M. Humidification of indoor air for preventing or reducing dryness symptoms or upper respiratory infections in educational settings and at the workplace. *Cochrane Database Syst. Rev.* **2021**, *12*, CD012219. https://doi.org/10.1002/14651858.cd012219.pub2.
56. Mardiana-Idayu, A.; Riffat, S.B. Review on heat recovery technologies for building applications. *Renew. Sustain. Energy Rev.* **2012**, *16*, 1241–1255. https://doi.org/10.1016/j.rser.2011.09.026.
57. Aridi, R.; Faraj, J.; Ali, S.; Gad El-Rab, M.; Lemenand, T.; Khaled, M. Energy Recovery in Air Conditioning Systems: Comprehensive Review, Classifications, Critical Analysis, and Potential Recommendations. *Energies* **2021**, *14*, 5869. https://doi.org/10.3390/en14185869.

58. Li, J.; Zmeureanu, R.; Ge, H. Simulation of energy impact of an energy recovery ventilator in Northern housing. *E3S Web Conf.* **2021**, *246*, 10005. https://doi.org/10.1051/e3sconf/202124610005.
59. Zhang, L.Z. Progress on heat and moisture recovery with membranes: From fundamentals to engineering applications. *Energy Convers. Manag.* **2012**, *63*, 173–195. https://doi.org/10.1016/j.enconman.2011.11.033.

Disclaimer/Publisher's Note: The statements, opinions and data contained in all publications are solely those of the individual author(s) and contributor(s) and not of MDPI and/or the editor(s). MDPI and/or the editor(s) disclaim responsibility for any injury to people or property resulting from any ideas, methods, instructions or products referred to in the content.